Sudan University of Science
and Technology
College of Graduate Studies

First Principles and Monte Carlo Simulation for Investigation of Phase Transition in $Au_{1-x}Cu_x$ Nano Alloys

المبادئ الأولية ومحاكاة مونت كارلو للتحقق من طور الانتقال من سبيكة الذهب والنحاس النانوية

A Thesis Submitted for Fulfillment of the Requirements for the Degree of Doctor of Philosophy in Physics

By

Mujahid Eldaw Jahelnabi Mohammed

Supervised By:

Associate Professor: Mohamed Hassan Eisa Salim

Co- Supervised By:

Associate Professor: Rawia Abdelgani Elobaid Mohammed

June - 2018

Dedication

This work is dedicated to those who support and encouraged me throughout the thesis

To my kind mother, and my great father

To my beloved little son and wife

To my brothers and sisters

To my relative and friends

This thesis would be incomplete without a mention of the support given by them.

Acknowledgement

First of all great thanks to Allah. Definitely, no work of value can be achieved without the help of Allah.

I want to thank my supervisor Dr. **Mohamed Hassan Eisa** (**M. H. Eisa**) for his exceptional support and care; he was the best teacher I ever had. A person who did not only teach me physics, but also taught me how to be a better human being. He spent so much time with each of us students to make sure we get the proper education and skills that we need, and the only thing he expected us to do in return was to learn, to teach him more when we can, and do the same for our students in the future.

I owe special thanks to my supervisor **Dr. Rawia Abdelgani Elobaid** for giving useful advice and fruitful suggestions.

I am indebted to Dr**. Mohammed Alshaikh Hamid Khalafalla** my future advisor, not only for his major contributions in creating the theoretical foundation of thermodynamic and phase diagrams or educating me about the current challenges of Phase Diagrams of Nano alloys, and motivating me to try to solve them, but also for his support and being a great inspiration in the past years, and I hope to continue with him in the coming years.

We are deeply indebted to **Physics Department**, College **of Science, Sudan University of Science and Technology** for moral support during our University years and in the writing of this study

المستخلص

حُسب طور الانتقال لجسيمات (سبيكة) الذهب والنحاس النانوية في مرحلة التكوين (الترتيب) وحدد توسع (تمدد) الكتلة الذي تمثله طاقات التكوين للعديد من التكوينات الذرية عن طريق حسابات المبادئ الأولية ومحاكاة مونت كارلو.

بعد ذلك، استخدم توسع (تمدد) الكتلة على أنه هاملتموني لحساب الخواص الثيرموديناميكية بواسطة محاكاة مونت كارلو لتوضيح طور الانتقال بين الحالات الأرضية (الاستقرار). وقد لوحظ بصورة واضحة تكوين هضاب (تدرجات) ذات اسطح مستوية ، مرتبط بالحالات الأرضية المحسوبة في مرحلة التكوين مقابل الجهد الكيميائي عند درجة حرارة منخفضة اقل من 100 كلفن ، وعند زيادة درجة الحرارة تشوهت او اختفت هذه التدرجات وهذا يدل على التحول في طور الذرات من المرتبة (المنظمة) الي طور غير مرتب (العشوائية) ، وقدرت درجة الحرارة الحرجة لهذا الانتقال بـ 100 كلفن ، بما يتفق مع اتجاه الدراسات السابقة التي وضحت أن درجة حرارة الانتقال بين اطوار المادة النانوية مرتبط بحجم سبيكة النانو وبالتالي ، فإن نتائجنا ذات صلة بالتطبيقات المتعلقة بترسب سبائك النانو المشتتة عند حجم صغير ~ 10 ذرات لكل سبيكة نانو.

تم تحسين جميع هياكل سبائك النانو هندسيا قبل تنفيذ الحسابات المذكورة أعلاه. حيث تضمن التحسين الهندسي حساب الخواص الميكانيكية للسبائك النانوية حيث أجريت عمليات محاكاة ذرية لدراسة ثابت الشبيكة والتمدد الحجمي أحداهما قائم على مشتقة ثابت الشبيكة والطاقة الكلية وأخري من حيث مشتقة الحجم والضغط المستخدم في كثير من الأحيان في المحاكاة وكلاهما اعطي نتائج وكميات متماثلة.

ABSTRACT

The calculation of phase transition in the configurational state (i.e. atomic arrangement) of Au_xCu_{1-x} nanoparticle (or Nano alloy) have been investigated by first principles and Monte Carlo calculations.

The cluster expansion represented by the formation energies of several atomic configurations have been determined from full potential, linearized augmented-plane-wave first-principle calculation. The cluster expansion was then used as a Hamiltonian for the Monte-Carlo calculation of the phase transition between the configurational ground states, "gs". Clear observation of plateau structures, associated with the calculated "gs, in the plane of the composition (x) versus the chemical potential have been observed at low temperatures < 100 K. The plateaus smeared out at higher temperatures, giving rise to the order-disorder transitions with temperature. The critical temperature for this transition was estimated at 100 K, consistent with the reported trend of the transition temperature with the Nano alloy size. Our results are thus relevant to applications concerning deposition of dispersed Nano alloys at small size ~ 10 atoms per Nano alloy. All the Nano-alloys structures were geometrically optimized before executing the above-mentioned calculations. The geometrical optimization involved the calculation of the mechanical properties of Nano alloys where we performed atomistic simulations to study the structure and Elastic constants for Au-Cu Nano-Alloy. Approaches used to compute the bulk modulus and lattice constant, one based on a definition in terms of the lattice parameter derivative of the total energy and another in terms of the volume derivative of the pressure often used in simulations. Both give quantitatively similar results.

List of Tables

List of Figures

List of Abbreviations

DFT	Density functional theory
DOS	Density of States
GGA	Generalized gradient approximation
HK	Hohenberg-Kohn
KS	Kohn-Sham
LAPW	Linearized augmented plane wave
LDA	Local density approximation
PAW	Projector augmented wave method
PP	Pseudopotential
PW	plane wave
FPLAPW	Full-Potential Linearized Augmented Plane-Wave
HF	Hartree-Fock
SCF	Self-Consistent-Field
EMC2	Easy Monte Carlo code
(ATAT)	alloy theoretic automated toolkit
MAPS	MIT Ab-initio Phase Stability
ASE	Atomic Simulation Environment

Table of Contents

CHAPTER 1: INTRODUCTION

1.1 Motivation

The combination of gold and copper is a good way to reduce the cost of gold and improve copper instability. Thanks to the form control the synergy of these two metals can be better exploited[1].

The Gold Copper Nano alloys are used for fuel cells, solar cells, batteries and capacitors in the power industry; it is also widely used in cancer therapy in the medicine industry, most of these uses depend mainly on thermal properties depending on the laws of thermodynamics and statistical physics.

This thesis reviews recent advances in our understanding of how temperature affects the structure and phase of multi metal Nanoparticles. The disorder order and melting phase transitions are strongly altered in nanoscale systems, and we describe how they can potentially affect future phase diagrams. The potential of Nano alloys in these diverse fields of application originates from the twin influence of size and composition and should be matched with the dual complexity of nanoparticles in general, with their specific size-dependent properties, together with alloys with their composition dependent properties. A question of fundamental importance with Nano alloys is that of stability, especially considering the wide variety of synthetic methods based on different physical or chemical techniques and which can produce compounds essentially identical in size and composition but with very different structures.

1.2 Importance of The Thesis

This thesis addresses the central challenge of Nano scale science: the need for fundamental understanding of how nanomaterials grow and for control of the growth environment, in order to synthesize materials with new or greatly enhanced properties at attractive rates we will focus our attention only on thermodynamic properties of this wide field.

In this thesis, we study the thermal properties of gold-copper Nano-alloy for its great importance in the field of medicine, especially cancer treatment.

1.3 Problem of the Thesis

First, the size (diameter and length) is rather small, prohibiting the application of well-established testing techniques. Tensile and creep testing require that the size of the sample be sufficiently large to be clamped rigidly by the sample holder without sliding. This is impossible for one-dimensional nanomaterials using conventional means. Second, the small size of the nanostructure makes their manipulation rather difficult, and specialized techniques are needed for picking up and installing individual nanostructures. Therefore, new methods and methodologies must be developed to quantify the properties of individual nanostructures.

1.4 Objectives of The Thesis

- he aim of the present thesis is derive a general expression for the equilibrium conditions at a solid interface of Gold - Copper Nano alloys.

- nderstand and control such effects in order to design artificially structured of nanomaterial's with new combinations of properties.
- alculation of phase transition in the configurational state of Au_xCu_{1-x} nanoparticle
- ompute the bulk modulus and lattice constant of Au_xCu_{1-x} nanoparticle

1.5 Scope of The Thesis

The thesis scope is organized into four chapters. Chapter one introduction, it consists of introduction, importance, problem, objectives and the scope, Chapter two deals with theoretical background and methodology, Chapter three is devoted to materials and methods employed in this work, Chapter four presents results and discussion.

CHAPTER 2: THEORETICAL BACKGROUND

2.1 Phase Diagram of Bulk Gold–Copper Alloys

The gold-copper (Au-Cu) system is great importance in industry, medicine, energy sources and many other applications.

The phase equilibria were extrapolated at low temperature and a condensed phase diagram was drawn for the Au-Cu system to be compatible with the third law of thermodynamics [2].

The system forms continuous solid solutions whose melting curve has a minimum at 44 % Cu and 910°C. The solid solutions are arranged to separate three phases of variable composition whose compositions are narrowed at the interface to the stoichiometric compounds Au_3Cu, AuCu and $AuCu_3$[3]. The temperatures at which the regions of homogeneity of these phases shrink sharply are, according to the thermodynamic simulations of Wei et al [4].

2.2 Nanoalloys Clusters

There are remarkable uses of precious metals in various technologically important fields because of their excellent catalytic, electronic and magnetic properties[5]. An improvement in properties is possible when two or more of these metals are combined [6]. The use of Nano-alloys has been reported since the 19th century, when Michael Faraday was studying Radioactivity but without a clear understanding of physical properties[7]. Advancement in methods and characterization made it possible for modern research to utilize the diversities in Nano alloy compositions[8]. and chemical ordering: intermetallic, random, non-random or phase segregation[9], in addition to size, atomic order and structure.

The clusters of Nano-alloys are also interesting because they may have structures and properties distinct from those of pure elementary clusters[10]. There are also examples of pairs of elements (such as Fe and Ag) that are not miscible in the bulk phase but that mix easily into finite groups[11].

A series of theoretical studies that mainly use empirical many-body potentials have been performed on intermetallic clusters [12]. Calculations based on functional density theory (DFT) were used for the study of bimetallic clusters [13, 14].

2.2.1 Gold–Copper Nano Alloy Clusters

The ‘‘noble metals’’, copper, silver and gold, occur naturally as the free metals, but they invariably have trace amounts of other noble metals incorporated into their lattices. Their similar electronegativity's and $d^{10}s^{1}$ electronic structures facilitate the alloying of these elements in the solid state[15]. In addition to extensive investigations of Au-Cu alloy phases in recent years, a number of experimental and theoretical studies on Au –Cu Nano alloys have been conducted. Of the Gold-based series studied in this work, Gold-Copper is the only binary for which the average potential agrees with the Density functional theory predictions. For both compositions of the clusters, In addition, a qualitative agreement is also observed for lower weightings for the parameter sets I–II.

2.2.2 Application of Gold–Copper Nanoalloys

The unique physical and chemical properties of precious metal nanoparticles have allowed these materials to be used as valuable tools in a variety of disciplines[16, 17]. Many of these applications

depend on the ability to intelligently modify the material shape, composition and structure[18].

In this thesis, we explain our recent contributions to the development and application of complex nanomaterials, specifically Gold-Copper Nano-alloy.

The unique thermal properties of nanoparticles have made them attractive targets for a wide range of applications that include communications[19], alternative energy[20], molecular sensing[21], In addition, spectroscopy[22], as well as medical imaging, detection, and therapy[22]. Such diverse applications require the ability to precisely tune the plasmonic properties[23]. which depend sensitively on particle morphology[24, 25].

2.3. Basic Aspects of Thermodynamics

There are several ways to get a solid system can exist in a variety of chemical and crystallographic arrangements or phases. We can define the phase as a homogeneous region in a liquid or a solid, with a characteristic atomic arrangement and a chemical composition[26].The different forms of the state or composition of the material depends on the thermodynamic variables (pressure, temperature and installation of the alloy, etc.)different phases or mixtures of phases are stable (the equilibrium state)[27]. Phase stability and phase transformation are critical to the design, behavior, and performance of the Alloy[28]. Equilibrium is always the combination of phases and compositions that is produced by minimizing Gibbs' overall free energy. [29, 30].

2.3.1 Equilibrium

Phase transformations occur in o rder to lower the energy of a system to achieve equilibrium[31]. So a system is said to be in equilibrium when it is most stable and shows no desire to change, and possesses the lowest possible energy[31, 32].

2.3.2 Internal Energy and First Law of Thermodynamics

The internal energy of a system is the sum of the potential and kinetic energies of all parts of the system[33]. If the system is subject to change from one state to another state, it is accompanied by an increase in internal energy (dU) change is brought about by the extraction of heat (δq) from the surroundings, and simultaneous performance of work (δw) by the system on the surroundings[34]. The First Law of Thermodynamics (energy can neither be created nor destroyed) states that the Increase in internal energy dU is [35, 36]

$$dU = \delta q - \delta W \tag{2.1}$$

The symbol d is used for a change in a state quantity or exact differential while the symbol 'δ' is used for a non-state change or inexact differential. At constant pressure, the First Law becomes

$$dU = \delta q - PdV \tag{2.2}$$

And at constant volume

$$dU = \delta q \tag{2.3}$$

2.3.3 Heat Content or Enthalpy

The enthalpy is the total internal and external energy of the system [37], given by the equation

$$H = U + PV \tag{2.4}$$

Thus, the differentiation of equation (2.4) give us:

$$dH = dU + PdV + VdP$$

From equation (2.2) $\delta q = dU + PdV$ so,

$$dH = \delta q + VdP \quad (2.5)$$

At constant pressure, VdP $=$ 0 so equation (2.5) gives

$$dH = \delta q \quad (2.6)$$

And at constant volume equation (2.4) reduces to

$$dH = dU \quad (2.7)$$

2.3.4 Heat Capacity (C)

The heat capacity of a substance is the heat required to raise the temperature, T, of unit mass by one degree, K [38], and is given by

$$C = \frac{\delta q}{dT}$$

at constant volume

$C = C_V = \left(\frac{\delta q}{dT}\right)_V = \frac{dU}{dT}$(Since from eq. (2.3) $\delta q = dU$,at constant volume)

at constant pressure

$$C = C_P = \left(\frac{\delta q}{dT}\right)_P = \frac{dH}{dT} \quad (2.8)$$

(Since from eq. (2.6) $\delta q = dH$, at constant pressure)Therefore

$$dH = C_P dT \quad (2.9)$$

And the variation of enthalpy with temperature is given by:

$$\int_{T_1}^{T_2} dH = \int_{T_1}^{T_2} C_P dT \quad (2.10)$$

$$H_{T_2} = H_{T_1} + \int_{T_1}^{T_2} C_P dT \quad (2.11)$$

Conventionally, the enthalpy of a pure substance in its standard state (i.e. most stable state) is defined to be zero at 298.16 K. So equation (2.11) can be written as:

$$H_T = \int_{298}^{T} C_p dT \tag{2.12}$$

$$H_T = \int_{298}^{T} (a + bT + cT^2) dT$$

$$H_T = \int_{298}^{T} \left[\sum C_{\ P;Products} - \sum C_{\ P;Reactants} \right] dT$$

And where a phase change occurs in the temperature range of interest

$$H_{T_2} = H_{T_1} + \int_{T_1}^{T'} C_P' dT + H_t + \int_{T''}^{T_2} C_P'' dT$$

Where C_P' and C_P'' are the heat capacities before and after transformation respectively.

H_{T_1} = Enthalpy at standard temperature.

H_{T_2} = Enthalpy at high temperature in question.

T' = Transformation temperature.

H_t = Enthalpy change at transformation.

2.3.5 Entropy and Second Law of Thermodynamics

Entropy can be considered from two points of view. One is an atomistic mechanical approach in which it is the measure of the randomness of a system[39]. The other is a thermodynamically approach according to which entropy arises from a consideration of the conditions under which heat can be converted into work (e.g. Carnot cycle)[40]. Mathematically entropy (S) is given by:

$$dS = \frac{\delta q}{T} \tag{2.13}$$

$dS = \frac{dH}{T}$ (At constant pressure)

And for a reversible change of state

$$S_{T_2} - S_{T_1} = \Delta S = \int_{T_1}^{T_2} \frac{\delta q}{T} \quad (2.14)$$

To give a fixed reference point the entropy of a pure substance at 0 K is taken to be zero (Third Law of Thermodynamics). Therefore, the entropy at T K is given by:

$$S = \int_0^T \frac{\delta q}{T}$$

Since at constant pressure $\delta q = dH = C_P dT$.so,

$$s = \int_0^T \frac{C_P}{T} dT \quad (2.15)$$

The consideration of an isolated system leads to an important conclusion. The entropy of such a system either remains constant ($dS = 0$) or increases ($dS > 0$). The entropy remains constant when the system is in an equilibrium state[40]. If it is not, the entropy increases until equilibrium is reached. This is an expression of the Second Law of Thermodynamics that the entropy in an isolated system tends to a maximum to gain stability (equilibrium)[41].

So when $dS = 0$ reaction is in equilibrium.

$dS > 0$ Reaction will occur spontaneously.

$dS < 0$ Reaction is impossible.

2.3.6 Gibbs Free Energy

Under isobaric conditions, any system undergoes a change to stabilize itself, and it is Gibbs free energy given as defines the stability of a system [2]:

$$G = H - TS \quad (2.16)$$

Where H = Enthalpy; T = temperature; S = Entropy and

$$\Delta G = \Delta H - T\Delta S \quad (2.17)$$

At constant temperature and pressure, a closed system (i.e. fixed mass and composition) will be in equilibrium if it has the lowest possible value of Gibbs free energy ($dG = 0$)[42].When a change occurs in a system, it is an attempt to minimize the overall energy of the system to attain stability. Equation (2.16) shows that the lowest possible value of G (highest stability) is only possible with a lower value of enthalpy (internal energy) and a higher value of entropy. The necessary criteration for any transformation is:

$\Delta G = G_2 - G_1 < 0$

Where $G_1$is initial and G_2 is a final stage, Equation (2.16) can be written in differential form as:

$$dG = dH - Tds \quad (2.18)$$

Now (i) If $\Delta \boldsymbol{G}$= 0 (i.e.$dH - TdS = 0$) the system is in equilibrium and there will be no phase change. Since $dH = C_P dT$,so at equilibrium:

$C_P dT - TdS = 0$ *or* $C_P dT = TdS$

(ii) If ΔG< 0, then change will occur

(iii) IfΔG> 0, the process is impossible

2.3.7 Helmholtz Free Energy

The stability of any system at constant volume is defined by the Helmholtz free energy[42]. The Helmholtz energy is defined as[43]:

$A = U + TS$

Where A is the Helmholtz free energy

From equation (2.2) $dU = \delta q - PdV$so,

Applying the product rule for differentiation

to $d(TS) = T\,dS + S\,dT$, we have

$$dU = d(TS) - SdT - PdV \tag{2.19}$$

And

$$d(U - TS) = -SdT - PdV$$

The definition of $A = U - TS$ enables to rewrite this as

$$d(A) = -SdT - PdV \tag{2.20}$$

2.3.8 The Kinetics of Phase Equilibria

The thermodynamic functions only describe whether a reaction will occur or not[44]. So it can therefore be used to calculate the driving force for transformation (i.e.$\Delta G = G_2 - G_1 < 0$), but it will not tell how fast this transformation will proceed. This belongs to the science of kinetics.

2.4 Equilibrium Phase Diagrams

One of the most important sources of information regarding a material system is the phase diagram, In which phase composition and phase stability are displayed as a function of temperature, composition and pressure[32]. These diagrams are usually plotted with temperature in degrees Centigrade, as the ordinate and alloy composition in atomic percent (or weight percent) as the abscissa[45]. Ideally, the phase diagram will show the relationship under equilibrium conditions[46]. Equilibrium conditions can be achieved by extremely slow heating and cooling, so that if a phase change does occur, sufficient time is allowed[47]. The change of phase depends upon the rate at which the alloy is heated or cooled[48]. Basically the task of a phase diagram is to summarize all phase changes which take

place, at equilibrium, in the system as temperature changes[31]. However a phase diagram will not provide any information on the reaction rate, and also it does not give any information on the possible existence of non-equilibrium phases, such as marten site In Hon alloys and some other alloys[49, 50]. Thermodynamically, a phase diagram may be regarded as a manifestation of the thermodynamic state of the system[51].

In this Thesis , the condition of thermodynamic equilibrium for a closed one phase ”solid” system leads to the usual conditions (mechanical equilibrium, homogeneous temperature and equal chemical potentials) and also to surface conditions (thermal, chemical and mechanical equilibrium).

2.4.1 Advantages of Phase Diagrams

Phase diagrams are maps (for solids, most often of temperature vs composition) indicating which phases are present at equilibrium for the given conditions[52]. If the thermodynamic quantities that are used to calculate the free energy are known experimentally, the phase diagrams can be calculated by one of many methods[53].

The use of phase diagrams for recording phase changes in alloys offers three advantages[32].

1. The conditions under which phase changes occur can be recorded simply and clearly for a large number of alloy compositions in a relatively small space.
2. The existence of certain rules of construction greatly reduces the number of experimental observations necessary to determine the phase relationships that exist in a whole series of alloys.

3. The recognition of quasi relationships between the constitution of alloys and their structure and properties makes the phase diagram an invaluable guide in the control of metallurgical processes.

2.4.2 Free Energy of a Binary System

Consider atoms A and B, which have the same crystalline structure, which can be mixed in any proportions to obtain a solid solution having the same crystalline structure[54]. Consider X_A and X_B are the mole fraction of A and B respectively, taking part so that: $X_A + X_B = 1$; then the total free energy before mixing is given by

$$G_1 = X_A G_A + X_B G_B \quad (2.20)$$

Which is shown schematically In Fig 2.4, where G_A and G_B are the molar free energies of A and B respectively. And after mixing the free energy of the solution is:

$$G_1 = G_1 + \Delta G_{mix} \quad (2.21)$$

Where

$$\Delta G_{mix} = \Delta H_{mix} - T\Delta S_{mix} \quad (2.22)$$

Where ΔH_{mix} is the heat of the solution (absorbed or evolved) and represents the difference in internal energy before and after mixing. Also ΔS_{mix} is the difference of the entropy between the mixed and unmixed state. The equation (2.20) becomes:

$$G_2 = G_{alloy} = X_A G_A + X_B G_B + \Delta G_{mix} \quad (2.23)$$

2.5 Order-Disorder Transformations

In alloys, the phase transformations can further be classified by whether they are clustering or ordering, this is measured by the ordering energy:

$$w = V_{AB} - \frac{V_{AA} + V_{BB}}{2} \tag{2.24}$$

Where the V are bond energies, when $w > 0$, clustering is favored, and when $w < 0$ ordering is favored.

An ordered compound has at least two sub-lattices, occupied by different chemical species. The degree of order can be measured by the two different parameters. The long range order parameter S and the short range order parameter σ.

The long-range order parameter S is given by

$$S = \frac{P_{aa} + x_a}{1 - a} \tag{2.25}$$

Where P_{aa} is the probability of finding an atom of type a on an "a" sub lattice site, and is the overall concentration of a in the alloy. In a perfectly ordered compound the probability of finding an "a" atom in an "a" site is 100% so$P_{aa} = 1$and $S = 1$. In a perfectly disordered compound the probability of finding an "a" atom at an "a" site is purely random (i.e. the atoms are evenly mixed in the lattice) and thus$P_{aa} = x_a$, so that $S = 0$.

The short-range order parameter is given by

$$\sigma = \frac{N_{ab} - N_{ab}^{dis}}{N_{ab}^{ord} - N_{ab}^{dis}} \tag{2.26}$$

where $N_{ab}$is the number of *a-b* pairs in the compound, $N_{ab}^{dis}$is the number of *a-b* pairs in the perfectly disordered compound, and $N_{ab}^{ord}$is the number of *a-b* pairs in the perfectly ordered compound, resulting again in an order parameter of $\sigma = 1$ for a perfectly ordered material and $\sigma = 0$ for perfectly disordered material.

Both parameters describe the state of chemical order of the material, but in general, the long-range order parameter is more accessible experimentally. The classical means of detection of long-range order is

by the presence of super lattice reflections, which are extinguished when the long-range order parameter goes to zero.

2.6. Density Functional Theory (DFT)

The idea in Density Functional Theory (DFT) is to abandon the handling of wave functions and replace them with electronic densities that can be measured laboratory[55]. The motive behind this is to reduce the number of variables in the calculations.

2.6.1 The Schrodinger Equation

The aim of most approaches in solid-state physics is the solution of the time-independent, non-relativistic Schrodinger equation[56]

$$\widehat{H}\psi_i\left(\vec{x}_1, \vec{x}_2 \ldots\ldots, \vec{x}_N, \vec{R}_1, \vec{R}_2, \ldots\ldots \vec{R}_M\right) = E_i\psi_i\left(\vec{x}_1, \vec{x}_2 \ldots\ldots, \vec{x}_N, \vec{R}_1, \vec{R}_2, \ldots\ldots \vec{R}_M\right) \quad (2.27)$$

$\widehat{H}$ Is the Hamiltonian for a system consisting of M nuclei and N electrons.

$$\widehat{H} = -\frac{1}{2}\sum_{i=1}^{N}\nabla_i^2 - \frac{1}{2}\sum_{A=1}^{M}\frac{1}{M^A}\nabla_A^2 - \sum_{i=1}^{N}\sum_{A=1}^{M}\frac{Z_A}{r_{iA}} + \sum_{i=1}^{N}\sum_{j>i}^{N}\frac{1}{r_{ij}} + \sum_{A=1}^{M}\sum_{B>A}^{M}\frac{Z_A Z_B}{R_{AB}} \quad (2.28)$$

Here, A and B run over the M nuclei while i and j denote the N electrons in the system.

The first two terms describe the kinetic energy of the electrons and nuclei. The other three terms represent the attractive electrostatic interaction between the nuclei and the electrons and repulsive potential.

The Born-Oppenheimer approximation is based on the observation that electrons move much faster and weigh much less than the nuclei[57]. It assumes the electronic motion and nuclear motion can be decoupled and that the electrons are in equilibrium with nuclei. In the Born Oppenheimer approximation, the electronic wave function depends on only the nuclear position so the kinetic energy of the nuclei can be neglect in the Hamiltonian. Therefore, electrons has a constant potential energy, and the total electronic Hamiltonian becomes

$$\hat{H}_{elec} = -\frac{1}{2}\sum_{i=1}^{N}\nabla_i^2 - \sum_{i=1}^{N}\sum_{A=1}^{M}\frac{Z_A}{r_{iA}} + \sum_{i=1}^{N}\sum_{j>i}^{N}\frac{1}{r_{ij}}$$
$$= \hat{T} + \hat{V}_{Ne} + \hat{V}_{ee} \qquad (2.29)$$

The solution of the Schrödinger equation with $\hat{H}_{elec}$ is the electronic wave function ψ_{elec} and the electronic energyE_{elec}.

$$\hat{H}_{elec}\psi_{\text{elec}} = E_{elec}\psi_{\text{elec}} \qquad (2.30)$$

The total energy E_{tot} is then the sum of electronic energy $E_{elec}$and the constant nuclear repulsion term E_{nuc}.

$E_{tot} = E_{elec} + E_{nuc}$ Where

$$E_{nuc} = \sum_{A=1}^{N}\sum_{B>1}^{M}\frac{Z_A Z_B}{R_{AB}} \qquad (2.31)$$

2.6.2 The Variation Principle for the Ground State

When a system is in the state , the expectation value of the energy is given by

$$E[\psi] = \frac{\langle\psi|\hat{H}|\varphi\rangle}{\langle\psi|\psi\rangle}$$

Where

$$\langle\psi|\hat{H}|\psi\rangle = \int \psi^* \hat{H}\psi d\vec{x} \tag{2.32}$$

The variation principle states that the energy computed from a guessed ψ is an upper bound to the true ground-state energyE_0 [58]. Full minimization of the functional $E[\psi]$ with respect to all allowed N-electrons wave functions will give the true ground state $\psi_0$and energy $[\psi_0] = E_0$; that is

$$E_0 = min_{\psi\to N} E[\psi] = min_{\psi\to N}\langle\psi|\hat{T} + \hat{V}_{Ne} + \hat{V}_{ee}|\psi\rangle \tag{2.33}$$

For a system of N electrons and given nuclear potential,V_{ext} the variational principle defines a procedure to determine the ground-state wave functionψ_0, the ground-state energy$E_0[N, V_{ext}]$, and other properties of interest. In other words, the ground state energy is a functional of the number of electrons N and the nuclear potentialV_{ext}:

$$E_0 = E[N, V_{ext}] \tag{2.34}$$

2.6.3 The Hartree-Fock Approximation

Suppose that ψ_o (the ground state wave function) is approximated as an anti-symmetrized product of N orthonormal spin orbital's $\psi_i(\vec{x})$, each a product of a spatial orbital $\phi_k\vec{r}$(~r) and a spin function $\sigma(s) = \alpha(s)$ or $\beta(s)$ the Slater determinant

$$\psi_o \approx \psi_{HF} = \frac{1}{\sqrt{N!}}\begin{vmatrix} \psi_1(\vec{x}_1) & \psi_2(\vec{x}_1) & \cdots & \psi_N(\vec{x}_1) \\ \psi_1(\vec{x}_2) & \psi_2(\vec{x}_2) & \cdots & \psi_N(\vec{x}_2) \\ \vdots & \vdots & \cdots & \dots \\ \psi_1(\vec{x}_N) & \psi_2(\vec{x}_N) & \cdots & \psi_N(\vec{x}_N) \end{vmatrix} \tag{2.35}$$

The Hartree-Fock approximation is the method whereby the orthogonal orbital's$\psi_i$are found that minimize the energy for this determinant form ofψ_i

$$E_{HF} = min_{(\psi_{HF\to N})} E[\psi_{HF}] \tag{2.36}$$

The expectation value of the Hamiltonian operator with ψ_{HF} is given by

$$E_{HF} = \langle \psi_{HF} | \hat{H} | \psi_{HF} \rangle = \sum_{i=1}^{N} H_i + \frac{1}{2} \sum_{i,j}^{N} (J_{ij} - K_{ij}) \quad (2.37)$$

$$H_i = \int \psi_i^*(\vec{x}) \left[-\frac{1}{2} \nabla^2 - V_{ext}(\vec{x}) \right] \psi_i(\vec{x}) d(\vec{x}) \quad (2.38)$$

Defines the contribution due to the kinetic energy and the electron-nucleus attraction and

$$J_{ij} = \iint \psi_i(\vec{x}_1) \psi_i^*(\vec{x}_1) \frac{1}{r_{12}} \psi_j^*(\vec{x}_2) \psi_j(\vec{x}_2) d\vec{x}_1 d\vec{x}_2 \quad (2.39)$$

$$K_{ij} = \iint \psi_i^*(\vec{x}_1) \psi_j(\vec{x}_1) \frac{1}{r_{12}} \psi_i(\vec{x}_2) \psi_j^*(\vec{x}_2) d\vec{x}_1 d\vec{x}_2 \quad (2.40)$$

The integrals are all real, and $J_{ij} \geq K_{ij} \geq 0$. The J_{ij} are called Coulomb integrals the K_{ij} are called exchange integrals. We have the property J_{ii}=K_{ii}.

The variation freedom in the expression of the energy [Eq. (2.37)] is in the choice of the orbitals. The minimization of the energy functional with the normalization conditions $\int \psi_i^*(\vec{x}) \psi_j(\vec{x}) \, d\vec{x} = \delta_{ij}$ leads to the Hartree-Fock differential equations:

$$\hat{f} \psi_i = \epsilon_i \psi_i \, , i = 1,2, \ldots . , N \quad (2.41)$$

These N equations have the appearance of eigenvalue equations, where the Lagrangian multipliers ϵ_i are the eigenvalues of the operator $\hat{f}$. The Fock operator $\hat{f}$ is an effective one-electron operator defined as

$$\hat{f} = -\frac{1}{2} \nabla_i^2 - \sum_{A}^{M} \frac{Z_A}{r_{iA}} + V_{HF}(i) \quad (2.42)$$

The first two terms are the kinetic energy and the potential energy due to the electron-nucleus attraction. $V_{HF}(i)$ is the Hartree-Fock

potential, the average repulsive potential experience by the i'th electron due to the remaining N-1 electrons, and it is given by

$$V_{HF}(\vec{x}_1) = \sum_{j}^{N} \left(\hat{j}_j(\vec{x}_1) - \hat{K}_j(\vec{x}_1) \right) \tag{2.43}$$

$$\hat{j}_j(\vec{x}_1) = \int \left|\psi_j(\vec{x}_2)\right|^2 \frac{1}{r_{12}} d\vec{x}_2 \tag{2.44}$$

The Coulomb operator $\hat{j}$ represents the potential that an electron at position $\vec{x}_1$experiences due to the average charge distribution of another electron in spin orbitalψ_j.

The second term in Eq. (2.43) is the exchange contribution to the HF potential. It has no classical analog and it is defined through its effect when operating on a spin orbital:

$$\hat{K}_j(\vec{x}_1)\psi_i(\vec{x}_1) = \int \psi_j^*(\vec{x}_2) \frac{1}{r_{12}} \psi_i(\vec{x}_2) d\vec{x}_2 \, \psi_j(\vec{x}_1) \tag{2.45}$$

- The HF potential is non-local and it depends on the spin orbitals Thus, the HF equations must be solved self-consistently.
- The Koopman's theorem (1934) provides a physical interpretation of the orbital energies: it states that the orbital energy $\epsilon_i$is an approximation of minus the ionization energy associated with the removal of an electron from the orbitalψ_i,.i.e. $\epsilon_i \approx E_N - E_{N-1}^i = -IE(i)$.

2.6.4 The Electron Density

The electron density is the central quantity in DFT It is defined as the integral over the spin coordinates of all electrons and over all but one of the spatial variables ($\vec{x} \equiv \vec{r}, s$)

$$\rho(\vec{r}) = N \int \cdots \int |\psi(\vec{x}_1 \vec{x}_2, \ldots, \vec{x}_N)|^2 ds_1 d\vec{x}_2 \ldots d\vec{x}_N \tag{2.46}$$

$\rho(\vec{r})$ determines the probability of finding any of the N electrons within volume element $d\vec{r}$.Some properties of the electron density.
Some properties of the electron density:

- $\rho(\vec{r})$is a non-negative function of only the three spatial variables which vanishes at infinity and integrates to the total number of electrons:

$$\rho(\vec{r} - \infty) = 0 \qquad \int \rho(\vec{r})\, d\vec{r} = N \qquad (2.47)$$

- $\rho(\vec{r})$is an observable and can be measured experimentally, e.g. by X-ray diffraction.
- At any position of an atom, the gradient of $\rho(\vec{r})$ has a discontinuity and a cusp results:

$$\lim_{r_i A \to 0} [\nabla_r + 2Z_A]\bar{\rho}(\vec{r}) = 0 \qquad (2.48)$$

Where Z is the nuclear charge and $\bar{\rho}(\vec{r})$ is the spherical average of $\rho(\vec{r})$

- The asymptotic exponential decay for large distances from all nuclei

$$\rho(\vec{r}) \sim exp\left[-2\sqrt{2I}|\vec{r}|\right] \qquad (2.49)$$

I is the exact ionization energy

2.6.5 The Thomas-Fermi Model

The conventional approaches use the wave function ψ as the central quantity, since ψ contains the full information of a system. However, ψ is a very complicated quantity that cannot be probed experimentally and that depends on 4N variables, N is the number of electrons.

The Thomas-Fermi model: the first density functional theory

- Based on the uniform electron gas, they proposed the following functional for the kinetic energy

$$T_{TF}[\rho(\vec{r})] = \frac{3}{10}(3\pi^2)^{2/3}\int \rho^{5/3}(\vec{r})d\vec{r} \qquad (2.50)$$

- The energy of an atom is finally obtained using the classical expression for the nuclear-nuclear potential and the electron-electron potential

$$E_{TF}[\rho(\vec{r})] = \frac{3}{10}(3\pi^2)^{2/3}\int \rho^{5/3}(\vec{r})\,d\vec{r} - Z\int \frac{\rho(\vec{r})}{r}d\,\vec{r} + \frac{1}{2}\iint \frac{\rho(\vec{r}_1)\rho(\vec{r}_2)}{r}d\vec{r}_1 d\vec{r}_2 \qquad (2.51)$$

In order to determine the correct density to be included in Eq.(2.51), they employed a variational principle. They assumed that the ground state of the system is connected to the $\rho(\vec{r})$ for which the energy is minimized under the constraint of $\int \rho(\vec{r})d\vec{r} = N$.

2.6.6 The Hohenberg-Kohn Theorems

Density functional theory is based on the two Hohenberg-Kohn (HK) theorems [59] , as follow:

Theorem I: demonstrates that the electron density uniquely determines the Hamiltonian operator and thus all the properties of the system.

This first theorem states that the external potential $V_{ext}(\vec{r})$ is (to within a constant) a unique functional of $\rho(\vec{r})$since, in turn $V_{ext}(\vec{r})$ fixes $\hat{H}$we see that the full many particle ground state is a unique functional of $\rho(\vec{r})$

Let us assume that there were two external potential $V_{ext}(\vec{r})$and $V'_{ext}(\vec{r})$differing by more than a constant, each giving the same $\rho(\vec{r})$

for its ground state, we would have two Hamiltonians $\hat{H}$ and $\hat{H}'$ whose ground-state densities were the same although the normalized wave functions and would be different. Taking ψ' as a trial wave function for the $\hat{H}$ problem

$$E_0 < \langle\psi'|\hat{H}|\psi'\rangle = \langle\psi'|\hat{H}'|\psi'\rangle + \langle\psi'|\hat{H} - \hat{H}'|\psi'\rangle$$
$$= E_0' + \int \rho(\vec{r})\,[V_{ext}(\vec{r}) - V_{ext}'(\vec{r})]d\vec{r} \qquad (2.52)$$

Where E_0 and E_0' are the ground-state energies for $\hat{H}$ and$\hat{H}'$, respectively. Similarly, taking ψ

as a trial function for the $\hat{H}'$ problem

$$E_0' < \langle\psi|\hat{H}'|\psi\rangle = \langle\psi|\hat{H}|\psi\rangle + \langle\psi|\hat{H}' - \hat{H}|\psi\rangle$$
$$= E_0 + \int \rho(\vec{r})\,[V_{ext}(\vec{r}) - V_{ext}'(\vec{r})]d\vec{r} \qquad (2.53)$$

Adding Eq. (2.52) and Eq. (2.53), we would obtain $E_0 + E_0' < E_0' + E_0$, a contradiction, and so there cannot be two different $V_{ext}(\vec{r})$ that give the same $\rho(\vec{r})$ for their ground state.

Thus, $\rho(\vec{r})$ determines N and $V_{ext}(\vec{r})$ and hence all the properties of the ground state, for example the kinetic energy$T[\rho]$, the potential energy V$[\rho]$, and the total energy $E[\rho]$. Now, we can write the total energy as

$$E[\rho] = E_{Ne}[\rho] + T[\rho] + E_{ee}[\rho]$$
$$= \int \rho(\vec{r})\,V_{Ne}(\vec{r})d\vec{r} + F_{HK}[\rho] \qquad (2.54)$$

$$F_{HK}[\rho] = T[\rho] + E_{ee} \qquad (2.55)$$

This functional $F_{HK}[\rho]$ is the holy grail of density functional theory. If it were known we would have solved the Schrödinger equation exactly! And since it is an universal functional completely independent of the system at hand, it applies equally well to the hydrogen atom as to gigantic molecules such as, say, DNA!

$F_{HK}[\rho]$Contains the functional for the kinetic energy $T[\rho]$and that for the electron-electron interaction, $E_{ee}[\rho]$, The explicit form of both these functional lies completely in the dark, However, from the latter we can extract at least the classical part$T[\rho]$,

$$E_{ee}[\rho] = \frac{1}{2}\iint \frac{\rho(\vec{r}_1)\rho(\vec{r}_2)}{r_{12}} d\vec{r}_1 d\vec{r}_2 + E_{ncl}$$
$$= J[\rho] + E_{ncl}[\rho] \qquad (2.56)$$

E_{ncl}Is the non-classical contribution to the electron-electron interaction: self-interaction correction, exchange and Coulomb correlation

Theorem II: states that$F_{HK}[\rho]$, the functional that delivers the ground state energy of the system, delivers the lowest energy if and only if the input density is the true ground state density. This is nothing but the variation principle:

$$E_0 \leq E[\tilde{\rho}] = T[\tilde{\rho}] + E_{Ne}[\tilde{\rho}] + E_{ee}[\tilde{\rho}] \qquad (2.57)$$

In other words this means that for any trial density $\tilde{\rho}(\vec{r})$, which satis_es the necessary boundary conditions such as $\tilde{\rho}(\vec{r}) \geq 0$, $\int \tilde{\rho}(\vec{r}) d\vec{r}$=N, and which is associated with some external potential$\tilde{V}_{ext}$, the energy obtained from the functional of Eq. (2.54) represents an upper bound to the true ground state energy E_0.E_0 Results if and only if the exact ground state density is inserted in Eq. (2.50)

2.6.7 The Kohn-Sham Equations

We have seen that the ground state energy of a system can be written as

$$E_0 = min_{\rho \to N}\left(F[\rho] + \int \rho(\vec{r}) V_{Ne} d\,\vec{r}\right) \qquad (2.58)$$

Where the universal functional $F[\rho]$ contains the contributions of the kinetic energy, the classical Coulomb interaction and the non-classical portion:

$$F[\rho] = T[\rho] + J[\rho] + E_{ncl}[\rho] \quad (2.59)$$

Of these, only $J[\rho]$is known. The main problem is to find the expressions for $T[\rho]$ and $E_{ncl}[\rho]$.

The Thomas-Fermi model of section 2.6.5 provides an example of density functional theory. However, its performance is really bad due to the poor approximation of the kinetic energy. To solve this problem Kohn and Sham proposed in 1965 the approach described below.

They suggested to calculate the exact kinetic energy of a non-interacting reference system with the same density as the real, interacting one

$$T_S = -\frac{1}{2}\sum_i^N \langle\psi_i|\nabla^2|\psi_i\rangle \, \rho_S = \sum_i^N \sum_S |\psi_i(\vec{r}, S)|^2 = \rho(\vec{r}) \quad (2.60)$$

Where the ψ_i are the orbital's of the non-interacting system. Of course, T_S is not equal to the true kinetic energy of the system. Kohn and Sham accounted for that by introducing the following separation of the functional $F[\rho]$

$$F[\rho] = T_S[\rho] + J[\rho] + E_{XC}[\rho] \quad (2.61)$$

WhereE_{XC}, the so-called exchange-correlation energy is defined through Eq. (2.61) as

$$E_{XC}[\rho] \equiv (T[\rho] - T_S[\rho]) + (E_{ee}[\rho] - J[\rho]) \quad (2.62)$$

The exchange and correlation energy E_{XC} is the functional that contains everything that is unknown.

Now the question is: how can we uniquely determine the orbital's in our non-interacting reference system? In other words, how can we define a potential V_S such that it provides us with a Slater determinant, which is characterized by the same density as our real system? To solve this problem, we write down the expression for the energy of the interacting system in terms of the separation described in Eq. (2.61)

$$E[\rho] = T_S[\rho] + J[\rho] + E_{XC}[\rho] + E_{Ne}[\rho] \tag{2.63}$$

$$E[\rho] = T_S[\rho] + \frac{1}{2}\iint \frac{\rho(\vec{r}_1)\rho(\vec{r}_2)}{r_{12}} d\vec{r}_1 d\vec{r}_2 + E_{XC}[\rho] + \int V_{Ne}\ \rho(\vec{r}) d\vec{r}$$

$$= -\frac{1}{2}\sum_{I}^{N} \langle \psi_i | \nabla^2 | \psi_i \rangle + \frac{1}{2}\sum_{i}^{N}\sum_{j}^{N} \iint |\psi_i(\vec{r}_1)|^2 \frac{1}{r_{12}} \left|\psi_j(\vec{r}_2)\right|^2 d\vec{r}_1 d\vec{r}_2$$

$$+ E_{XC}[\rho] - \sum_{i}^{N} \int \sum_{A}^{M} \frac{Z_A}{r_{1A}} |\psi_i(\vec{r}_1)|^2 d\vec{r}_1 \tag{2.64}$$

The only term for which no explicit form can be given is E_{XC}. We now apply the variational principle and ask: what condition must the orbitals ψ_i fulfill in order to minimize this energy expression under the usual constraint $\langle \psi_i | \psi_j \rangle = \delta_{ij}$? The resulting equations are the Kohn-Sham equations:

$$\left(-\frac{1}{2}\nabla^2 + \left[\int \frac{\rho(\vec{r}_2)}{r_{12}} + V_{XC}(\vec{r}_1) - \sum_{A}^{M} \frac{Z_A}{r_{1A}}\right]\right)\psi_i = \left(-\frac{1}{2}\nabla^2 + V_S(\vec{r}_1)\right)\psi_i$$

$$= \epsilon_i \psi_i \tag{2.65}$$

$$V_S(\vec{r}_1) = \int \frac{\rho(\vec{r}_2)}{r_{12}} d\vec{r}_2 + V_{XC}(\vec{r}_1) - \sum_{A}^{M} \frac{Z_A}{r_{12}} \tag{2.66}$$

2.6.8 The Local Density Approximation (LDA)

The local density approximation (LDA) is the basis of all approximate exchange-correlation functional.

At the center of this model is the idea of a uniform electron gas.

This is a system in which electrons move on a positive background charge distribution such that the total ensemble is neutral.

The central idea of LDA is the assumption that we can write E_{XC}in the following form

$$E_{XC}^{LDA}[\rho] = \int \rho(\vec{r})\epsilon_{XC}\rho(\vec{r})d\vec{r} \tag{2.67}$$

Here, $\epsilon_{XC}\rho(\vec{r})$ is the exchange-correlation energy per particle of an uniform electron gas of density $\rho(\vec{r})$. This energy per particle is weighted with the probability $\rho(\vec{r})$ that there is an electron at this position. The quantity $\epsilon_{XC}\rho(\vec{r})$ can be further split into exchange and correlation contributions,

$$\epsilon_{XC}\big(\ \rho(\vec{r})\big) = \epsilon_X\big(\ \rho(\vec{r})\big) + \epsilon_C\big(\ \rho(\vec{r})\big) \tag{2.68}$$

The exchange part, X, which represents the exchange energy of an electron in a uniform electron gas of a particular density, was originally derived by Bloch and Dirac,

$$\epsilon_X = -\frac{3}{4}\left(\frac{3\rho(\vec{r})}{\pi}\right)^{1/3} \tag{2.69}$$

No such explicit expression is known for the correlation part.ϵ_C. However, highly accurate numerical quantum Monte-Carlo simulations of the homogeneous electron gas are available (Ceperly-Alder, 1980).

2.6.9 The Generalized Gradient Approximation (GGA)

The first logical step to go beyond LDA is the use of not only the information about the density $\rho(\vec{r})$ at a particular point $\vec{r}$ but to supplement the density with information about the gradient of the charge density $\nabla\rho(\vec{r})$ in order to account for the non-homogeneity of the true electron density. Thus, we write the exchange-correlation energy in the following form termed generalized gradient approximation (GGA).

$$E_{XC}^{GEA} = [\rho_\alpha, \rho_\beta] = \int f(\rho_\alpha, \rho_\beta, \nabla\rho_\alpha, \nabla\rho_\beta) d\vec{r} \qquad (2.70)$$

Thanks to much thoughtful work, important progress has been made in deriving successful GGA's. Their construction has made use of sum rules, general scaling properties, etc. In another approach, A. Becke introduced a successful hybrid functional:

$$E_{XC}^{hyb} = \alpha E_X^{KS} + (1-\alpha) E_{XC}^{GGA} \qquad (2.71)$$

WhereE_X^{KS}X is the exchange calculated with the exact KS wave function, $E_{XC}^{GGA}$is an appropriate GGA, and $\alpha$is a fitting parameter.

2.7 **Literature review**

In the late ninetieth and early twentieth centuries, the pioneer work in the determination of phase diagrams was made by Heycock and Neville, who determined the liquids curves for some binary alloys systems.

Also the work on ternary phase diagrams was started more or less In the same era, and the first 14 ternary diagrams were developed by C. A. R.3 Wright from 1888 to 1898. He developed his first ternary diagram of Pb-Sb-Sn in 1888. Early workers, in particular Heycock and Neville, determined phase diagrams, which have proved to be Surprisingly accurate in view of the lack of technology and development in apparatus

at that time. A lot of diagrams were produced in the first decade of the twentieth century. In the years 1905-1915 equilibrium phase diagrams for many alloy systems were published by the workers of the German school associated with the name of Tammann. In this period an average of 30 diagrams per annum were produced, but from 1916 to 1918 only four binary and two ternary diagrams were produced due to the interruption of work by the First World War. After the First World War, the general standard of equilibrium phase diagram work was raised largely in the British National Physical Laboratory, which was working under the guidance of Rosenhain, and produced diagrams associated with the names of Gayler, Haughton and Hanson. In 1922 again the output reached the pre-war level, and from 1925 it agaIn increased rapidly until shortly after the outbreak of the Second World War.

Mingjin Cui , etl [60] study's Phase Diagram of Continuous Binary Nano alloys: Size, Shape, and Segregation Effects Based on the size dependent cohesive energy model, developed a unified Nano-thermodynamic model to investigate the effects of the size, shape, and segregation on the phase diagrams of continuous binary Nano alloys.

F. Berthier , etl [61] studs Phase diagrams of nanoalloys: influence of size and morphology Based on The variation of the critical temperature with the length of all these nanoparticles is systematically studied using Monte Carlo simulations based on an Ising model. A non-monotonic variation of the critical temperature is observed as a function of the length. The maximal value of the critical temperature is reached when the length and the circumference of the nanoparticles are similar.

R. Mendoza-Cruz etl [62] studs Order–disorder phase transitions in Au–Cu nanocubes: from nano-thermodynamics to synthesis. this paper theoretically predicts the structural phase transitions between ordered and disordered

phases for the Au–Cu system by using nano-thermodynamics. Following the predictions, the suggested annealing temperatures have been carefully chosen and consequently, Au–Cu ordered nanocubes have been successfully synthesized through a solventless protocol.

CHAPTER 3: MATERIALS AND METHODS

3.1 Sample Description

Nanoparticles or Nano-alloys are microscopic objects having at least one dimension less than 100 nm. When the particle size reaches the nanoscale, the crystal boundary is destroyed or the atomic density changes. Due to this change in physical properties, the use of nanomaterials varies considerably in many fields of science and technology. Gold-copper (Au-Cu) nanoparticles have been regarded as valuable tools in a variety of disciplines.

Our objective in this thesis is to capture the thermodynamic properties of $Au_{1-x}Cu_x$ nanoparticles (Nano alloys).

For this purpose we have used a combination of first-principle density functional (DFT) and Monte-Carlo calculations. In DFT calculation, a periodic image of the atomic structure is generated to mimic the bulk structure. This is called a super-cell, i.e. the super-cell is repeated periodically to generate the bulk structure. For example, consider the hypothetical four atoms super-cell structure. A DFT program will generate many periodic images of this structure.

Now to simulate a nanoparticle we need to separate the periodic images of the super-cells by a vacuum to avoid the interaction between the periodic super-cells. Here, the period images of the nanoparticles are isolated from each other by the vacuum regions. This allows the DFT code to produce results pertinent to the nanoparticles rather than to the bulk structure. In our work, the Monte Carlo simulation cell consists of isolated Nano-alloys, hence, all the calculated thermodynamic properties are influenced by the isolated nan-alloys. Our results can thus be relevant to experimental work

associated with dispersed (isolated) Nano-alloys, such as those produced at an early stage of the Nano-alloy deposition

3.1.1 Thermal properties of Au-Cu Nano alloy

For most of these applications it is very instructive to thermodynamically characterize the active material. That is why thermodynamic phase diagrams are regarded as an important source of information in bulk material. Phase diagrams are maps (for solids, most often of temperature vs. composition) indicating which phases are present at equilibrium for the given conditions. However, thermal stability in nanoparticles are often different from the corresponding bulk material. Most often information about the thermodynamic properties of nanoparticles are obtained theoretically due to the relatively difficult experimental measurements of thermal stability of nanoparticles.

3.1.2 Mechanical properties of Au-Cu Nano alloy

Some mechanical properties of Nano alloys, such as strain, tensor, the shear constant, the hardness and the bulk modulus will aid a lot in the proper design of particles in specific applications. This thesis aims at the calculation of the mechanical properties of Au-Cu nanoparticles or Nano alloys, from the calculation of the lattice constant and bulk modulus by computational method pagane quantum espresso.

3.2 Computational Programs and Simulation

In this thesis, many simulation and computer programs were used to generate alloys and calculate their properties such as mechanical and thermal.

3.2.1 Atomic Simulation Environment (ASE)

We use ASE for structure optimization, molecular dynamics, handling constraints, nudged elastic band calculations, vibrational analysis, simulated STM images, calculation of Wannier functions, transport calculations and much more.

3.2.2 ELK-LAPW code

Elk is an all-electron full-potential linearised augmented plane-wave (LAPW) code for determining the properties of crystalline solids. It was developed originally at the Karl-Franken's. It is also extensively used for production, especially for materials which are particularly sensitive to the types of approximation used or for which pseudopotential methods are not appropriate. One aspect which is unique to Elk is that almost all features can be used in combination with each other, resulting in powerful and robust code.

The LAPW basis is constructed by partitioning space into spheres around atoms, called muffin-tins, and the remaining interstitial region. Linear combinations of atomic-like orbitals make up the basis functions in the muffin-tins and plane waves fill the interstitial region. At the boundary, the functions, and possibly their derivatives, are matched ensuring continuous or differentiable basis functions.

3.2.3 Quantum Espresso

Quantum Espresso is a variety of numerical methods & algorithms aimed at a chemically realistic modeling of materials from the Nano scale upwards, based on the solution of the density functional theory (DFT). It is an integrated suite of computer codes for electronic structure calculations and materials modeling based on

DFT, plane waves and pseudo potentials (norm conserving, ultra-soft and projector augmented wave) to represent the electron-ion interactions. The ESPRESSO stands for open Source Package for Research in Electronic Structure, Simulation &Optimization. The codes are constructed around the use of periodic boundary conditions, which allows for a straightforward treatment.

of infinite crystalline systems [63] . Quantum espresso can do several important basic computations such as, Calculation of the Kohn-Sham (KS) orbital's and energies for isolated systems, and of their ground state energies, Complete structural optimizations of the atomic coordinates ,ground state of magnetic or spin polarized systems,..etc.

3.2.4 The MAPS (MIT Ab-initio Phase Stability) code

Axel van de Walle with Professor Gerd Seder's developed the MAPS (MIT Ab-initio Phase Stability) code, which automatically builds mass expansion from the results of the initial principle calculations. MAPS consists of the following code: maps, corrdump, genstr, checkcell, kmesh, cv[64]. The MAPS and emc2 are parts of the open-source alloy theoretic automated toolkit (ATAT).

In this thesis The structures (lattice sites with various atomic configurations) were produced by the MIT Ab-initio Phase Stability (MAPS) code [65] from a parent lattice defined by the atomic sites for the 13 Au atoms nanoparticle.

3.2.5 Monte Carlo simulation

Axel van de Waale, together with Professor Mark Aasta of Northwestern University has, developed the Easy Monte Carlo code (EMC2), which automates the thermodynamic properties calculation via Monte Carlo

simulations of lattice models of the alloy[64]. EMC2 consists of the following code: emc2, phb.

In this thesis we used the Monte Carlo simulation to a representation of the structures energies was used as a Hamiltonian for the Monte-Carlo simulation, which was utilized to provide the thermodynamic phase structure. The monte-Carlo simulation was performed with the Easy Monte Carlo Code (emc2)

3.3 Computational methods

Figure 3.1. is a schematic flow chart showing the main computational stages for the calculation of the phase diagram of Au_xCu_{1-x} Nano-alloy, which consists of 13 atoms (see Figure 4.8 (a)). The first stage (1^{st} stage, Figure. 3.1) concerned with the optimization of the lattice constants for Au, Cu, and Au-Cu bulk materials. The determination of the bulk lattice constant was required in the 2^{nd} stage (Figure. 3.1) to generate the corresponding Nano-alloy. We used the full-potential code called Exciting to optimize the structures generated from the primitive lattices belonging to the cubic space group Fm-3 m for Cu, Au, and Au-Cu. In these calculations, the energy convergence threshold was 0.027 meV and the number of k points was uniformly distributed in $8 \times 8 \times 8$ grid. The geometry optimization results are shown in Figure. 4.7 (a) – (c). In these figures the calculated energies versus the volume were fitted to Murnghan equation of state shown by the solid lines, giving rise to the optimized lattice constants a_{Au} = 4.109 Å, $a_{Au\text{-}Cu}$ = 3.859 Å, and a_{Cu} = 3.564 Å corresponding to the minimum energy points in Figure 4.8 (a) – (c) respectively. Clearly the calculated lattice constants are consistent with the experimental ones: $a_{Au,}$exp = 4.078 Å, $a_{AuCu,exp}$ = 3.863 Å and a_{Cu},exp = 3.615 Å. Figure. 4.7 (d) shows that the lattice constants agree with Vegard's law [66] for binary

alloys, i.e. The calculated lattice constants (circles, Figure. 4.7 (d)) fits well to

$a_x = (1 - x)\, a_{Au} + x\, a_{Cu}$, where x is the material composition. For example, for x = 0.5, $a_{0.5} = (1\text{-}0.5)\, a_{Au} + 0.5\, a_{Cu} = 3.837$ Å ~ $a_{AuCu} = 3.859$ Å. Thus, we used a_x obtained from Vegard's law as an input for the code that generates the Nano-alloys (2nd stage, Figure. 3.1).

We point out that the structure relaxation (i.e. minimization of atom-atom forces) was not performed. However a relaxation test on one of the structures showed that the inter-atomic force was comparable with the program's default threshold value ~ 0.04 nm (Here, and for simplicity, we used the plane-wave code: Quantum Espresso.

After optimizing the lattice constants in the 1st stage (Figure. 3.1), we then used the optimized lattice constants with the Atomic Simulation Environment (ASE) to generate the Nano-alloy with 13 atoms by employing the Wulff-construction method incorporated with ASE. The generated Au nanoparticle is shown in Figure. 4.8 (a) where the cubic box (dashed lines) has a side $a_{Au} = 4.109$ Å, which is the lattice constant optimized in the 1st stage as discussed above. The Cu nanoparticle looks similar but with $a_{Cu} = 3.564$ Å.

In the 3rd stage (Figure. 3.1) we employed the cluster-expansion method [67] for the aim of the determination of the thermodynamic properties (e.g temperature-composition phase diagram) of $Au_{1-x}Cu_x$ Nano-alloy.

The structures (lattice sites with various atomic configurations) were produced by the MIT Ab-initio Phase Stability (MAPS) code from a parent lattice defined by the atomic sites for the 13 Au atoms nanoparticle (Figure. 4.9 (a)) with $a_{Au} = 4.109$ Å and placed in a corner of large empty box with a side a ~ 10 Å (e.g. see right inset of Figure. 4.9 (b)). Placing the $Au_{1-x}Cu_x$

Nano alloy in the empty box will isolate it from its periodic images generated by the energy calculation program, as we will discuss shortly.

A new structure ($Au_{1-x}Cu_x$) was automatically generated by MAPS immediately after the completion of the energy calculation of a given structure. The structures energies were calculated using the first-principle ELK-LAPW code which is a high precision all-electron density functional software. The ELK-LAPW energy convergence threshold was 0.027 meV, the uniform grid k-points were $2 \times 2 \times 2$ (we notice slight energy difference for denser grid), and the maximum reciprocal lattice vector was set to $rgkmax/R_{mt}$ with the input parameter rgkmax = 7 and R_{mt} defining the muffin-tin radius (radius of atomic potential as defined by the default setting of the ELK-LAPW program). The exchange-correlation functional for Au and Cu used in ELK-LAPW was the Generalized-Gradient-Approximation (GGA) of the type called Perdew-Burke-Ernzerhof for solids (PBEsol). The termination of the energy calculation and, hence, of the structure generation was decided after getting the following output message from MAPS:

"Among structures of known energy, true and predicted ground states agree. No other ground states of 13 atoms/unit-cell or less exist."

which indicated that agreement between the true (i.e calculated) and predicted (by MAPS) ground states (lowest energy structures), for a given concentration x, have been reached. These ground state structures, denoted as gs0, gs1, gs2 and gs3, are indicated along the convex hull (solid line) in the plane of the formation-energy versus concentration x as shown in Figure 4.8 (b). The insets of Figure 4.9 (b) show the atomic structures for these ground states. In Figure. 4.8 (b) the "known structures" (denoted as crosses) are the structures whose energies were calculated from first-principle.

Finally (4^{th} stage, Figure 3.1), a representation of the structures energies was used as a Hamiltonian for the Monte-Carlo simulation which was utilized

to provide the thermodynamic phase structure. The monte-Carlo simulation was performed with the Easy Monte Carlo Code (emc2). The emc2 simulation cell size was optimized at $10 \times 110 \times 110$ Å^3. Above this size no significant change in the thermodynamic property was observed, e.g. refer to Figure 4.9 (a) which shows the variance of concentration versus temperature with the emc2 size (indicated as "er", representing the radius of the sphere fitting inside the simulation cell) as a parameter. In fact, the emc2 simulation cell consists of many periodic Nano-alloy structures (e.g. like the ones shown in the inset of Figure 4.9 (c)). This allowed the Monte-Carlo code to produce the average values for the thermodynamic quantities over the entire cell. Since the periodic Nano-alloys are isolated from each other by a large empty space (see empty box with side a = 10 Å in the inset of Figure 4.9 (b)), then these averaged thermodynamic quantities were associated with the Nano-alloy. The rest of the main emc2 setting parameters were dmu = 1.1 meV (chemical potential step), and $dT = 10$ K (temperature step). It is worth mentioning that the MAPS and emc2 are parts of the open-source alloy theoretic automated toolkit (ATAT). Additionally, by chemical potential we mean the chemical potential difference between that for Au and Cu in the emc2 simulation cell. The chemical potential imposes the condition that allows for variation in the atomic concentration for fixed total number of atoms [68].

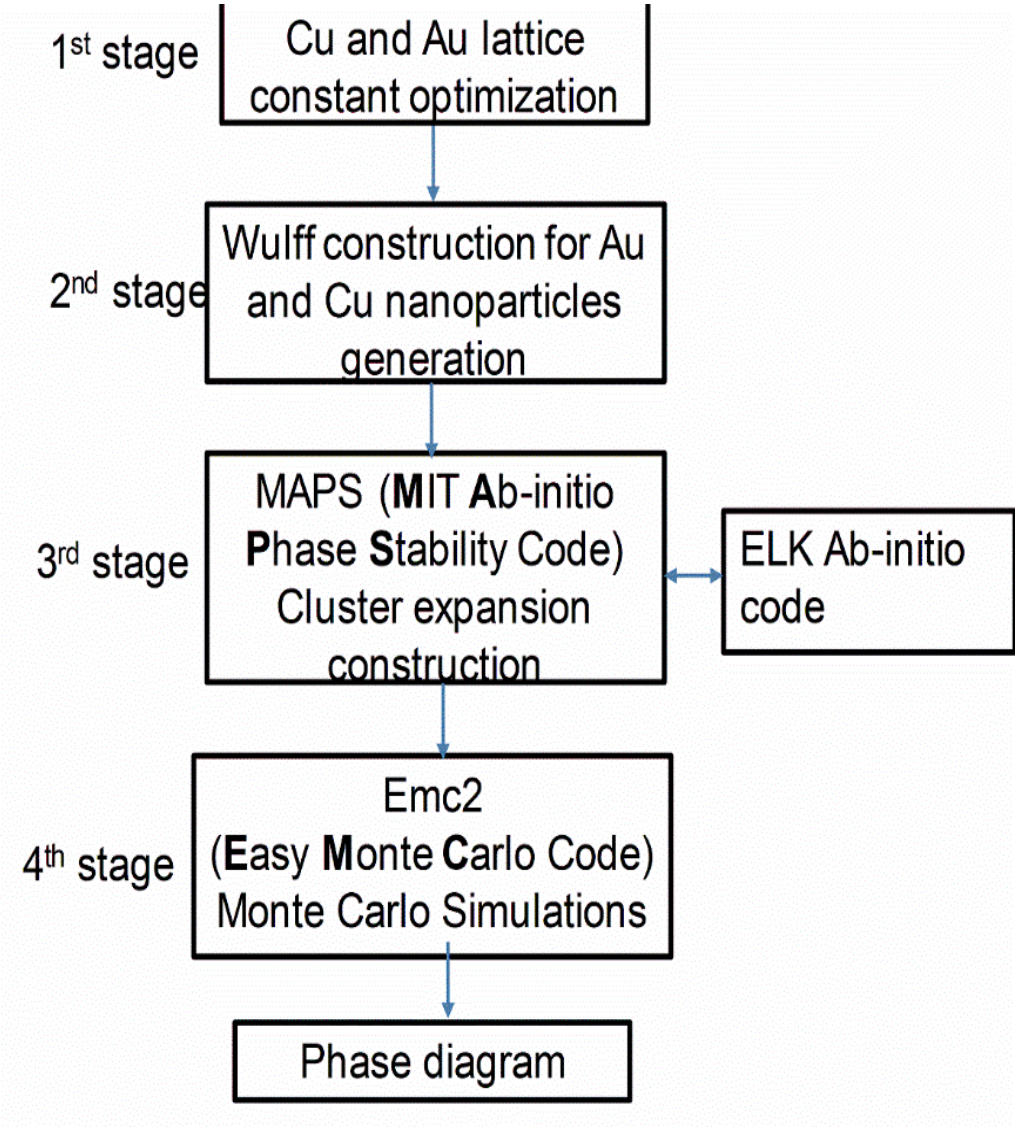

Figure 3.1: A schematic flow chart showing the main computational stages for the calculation of the phase diagram of AuxCu1-x Nano-alloy.

CHAPTER 4: RESULTS, DISCUSSION AND CONCLUSIONS

4.1 Results and discussion

In this thesis, mechanical and thermodynamic properties were calculated and the concentration on thermal properties was considered the basis of the thesis.

4.1.1 Results of the Mechanical properties

We first present the results for structural properties. In order to obtain the equilibrium volume, we calculated the total energy for the Au NPs, Cu NPs and Gold-Copper NPs by varying hydrostatically the volume and allowing fully relaxation of the ions. The results are shown in Figure (4.1 ,4.2, and 4.3) The equilibrium lattice parameter was found using the GGA functional. The calculated results for equilibrium lattice are summarized in the (Table 4.1).

We now turn the attention to the bulk modulus calculation. In order to obtain the equilibrium volume we calculated the pressure for the Au, Cu and Au-Cu NPs. The results are shown in Figure (4.4, 4.5 , and 4.6) . The bulk modulus K_0 was determined from the results of total energy change with respect to the hydrostatic variation of volume and fitted to the fourth-order Birch-Murnaghan equation of state. These results in bulk modulus as summarized in the Table 4.1.

4.1.2 Results of the Thermal properties

The Monte-Carlo simulation results are shown in Figure 4.9 (b) of the chemical potential ($\delta\mu$) as a function of the average Au concentration, x, with the temperature, T, as a parameter. The Monte-Carlo code (emc2) performed the calculations in a cell consisting of 11×11×11 (i.e. super-cell) structures associated with the respective ground state of interest. Figure 4.9 (c) shows an example of such a super-cell. Therefore, the concentration x in Figure 4.9 (b) corresponds to the average concentration over the entire super-cell. It is very important to emphasis here that our results in Figure 4.9 (b) are related to a large ensemble of non-interacting Nano-alloys (i.e each $Au_{1-x}Cu_x$ Nano-alloy consists of 13 atoms). This is because the super-cell was consisting of isolated Nano-alloys separated from each other by a vacuum box with size $a \sim 10$ Å (see right inset of Figure 4.9 (b).

In Figure 4.9 (b), as $\delta\mu$ increases, x changes from 0 (pure Cu) to 1 (pure Au). Additionally, at low temperatures (< 100 K), plateaus of stable atomic concentrations (horizontal plateaus labeled as P0, P1, P2 and P3) were observed. The plateaus P0, P1, P2, and P3 were belonging to the ground states gs0, gs1, gs2, and gs3, respectively. Generally, the x ranges (for all temperatures) associated with gs0, gs1, gs2, and gs3 are, respectively, indicated below the insets of Figure 4.9 (b) as $0 \leq x \leq 0.62$, $0.54 \leq x \leq 0.62$, $0.62 \leq x \leq 1$, and $0.76 \leq x \leq 1$. The plateaus of stability regions occurred at $x = 0$, 0.54, 0.77, and 1 within these ranges. These plateaus are reminiscent of those observed in Ref# [69] for Au-Pd Nano-alloy which were attributed to the shell felling effect associated with the progressive transfer of Au into the core shell as the chemical potential difference between Au and Pd increases. In contrast, our Nano alloy is only 13 atoms in size, hence, has no clear distinction between surface and core shells. Therefore, adding Au or Cu atoms to a Nano-alloy occurs in a discrete manner, leading to the

observed discrete jumps between the plateaus of stable x at $T < 100$ K. This is analogues to the case of discrete charging of a nano-device (e.g. a quantum dot), connected to electron reservoir terminals, which occurs one electron at a time whenever the reservoir's electro-chemical potential (or Fermi level) aligns with the narrow electro-chemical potential of the nano-device, leading to the stair-case pattern (plateaus) in the plane of the nano-device current versus the bias voltage.

However, as T increases, the plateaus gradually smear out as shown in Fig. 4.9 (b) at $T \sim 1000$ K (Red region). This smearing out can simply be attributed to the temperature broadening of $\delta\mu$, allowing for the ground states with similar space-groups (e.g. g s0, gs2, and gs3 are having m3-m space group symmetry) to coalesce at higher temperatures. That could explain why structures belonging to gs1 (having 4_2m symmetry, i.e. tetragonal based on atomic arrangement) were confined to $T < 300$ K (A careful look at Figure 4.9 (b) around $0.54 \leq x \leq 0.62$ would reveal this confinement).

We have also observed that the low-to-high temperature transition in Figure 4.9 (b) was accompanied by order-to-disorder transition as shown in Figure 4.10 (a), where the left panel shows a cross-section view of the Monte-Carlo (emc2) simulation cell belonging to gs2 (namely at $x = 0.62$) at 50 K with ordered atomic arrangements such that each Cu (dark sphere) is symmetrically surrounded by 12 Au atoms (golden spheres). The disordered arrangement at 1000 K can clearly be viewed in the right panel. Figure 4.10 (b) shows that, for gs2, x is almost fixed for $T < 100$ K then decreases after 100K. The region with nearly constant x are associated with the ordered phase. As T increases addition of more Cu atoms becomes favorable, enhancing the disordered phase. We have also attempted to further investigate this order-to-disorder transition through the evaluation

of the average (i.e. evaluated over entire emc2 cell) order-parameter, η [70], as a function of temperature for gs2 starting from $x = 0.62$ and $T = 0$ K. The result is illustrated in Figure 4.10 (c). Clearly $\eta \sim 1$ for $T < 100$ K. The descend in η within 40 K < T < 100 K is associated with the slight loss of Cu atoms (i.e. slight increase in x) as T increases from ~ 40 K to 100 K which can clearly be observed in Figure 4.10 (b). Above $T \sim 100$ K, x reduces (due to addition of Cu) while η increases and then reduces after $T \sim 500$ K. The partial increase in η below 500 K may be due to that the added Cu atoms reclaimed their atomic sites lost at 40 K < T < 100 K. However, this behavior may be compared with the results of figure 37 in [6] where the order-parameter is seen to monotonically reduces from 1 to 0 for bulk alloy only, whereas for the Nano alloys it exhibits regions of saturation which get wider for smaller Nano alloys. Therefore, we determine the order-disorder transition temperature for our Nano alloy to be ~ 100 K. We believe that this temperature is consistent with the report by Mendoza *et al* [62] who demonstrated that the order-disorder transition temperature for Nano alloy was smaller than that for the bulk. This may indicate that the transition temperature reduces with Nano-alloy size. In Mendoza *et al* [62] the average transition temperature ~ 300 K for Au-Cu Nano-alloy 10 nm in size. Our Nano-alloy is much smaller and exhibits ~ 100 K transition temperature, which may be regarded as consistent with the trend observed by Mendoza *et al*[62].

Even though the calculation of the transition temperature was performed in gs2, we anticipate that similar calculations in other ground states would lead to similar result. We also point out that η represents the long-range order parameter defined by equation 38 in [70]. Nevertheless, since our data in Figure 4.10 (b) and 4.10 (c) are consistent, we believe that using the

long-range order parameter to investigate our structures at the nanoscale level was acceptable.

Table 4.1: First principles structural and bulk modulus of Au, Cu and Au-Cu NPs.

Materials		$a_0(A^\circ)$	K_0 **(GPa)**
Au NPs		11.32277	11.3
Cu NPS		9.80072	12.0
Au-Cu NPs		11.00800	13.5

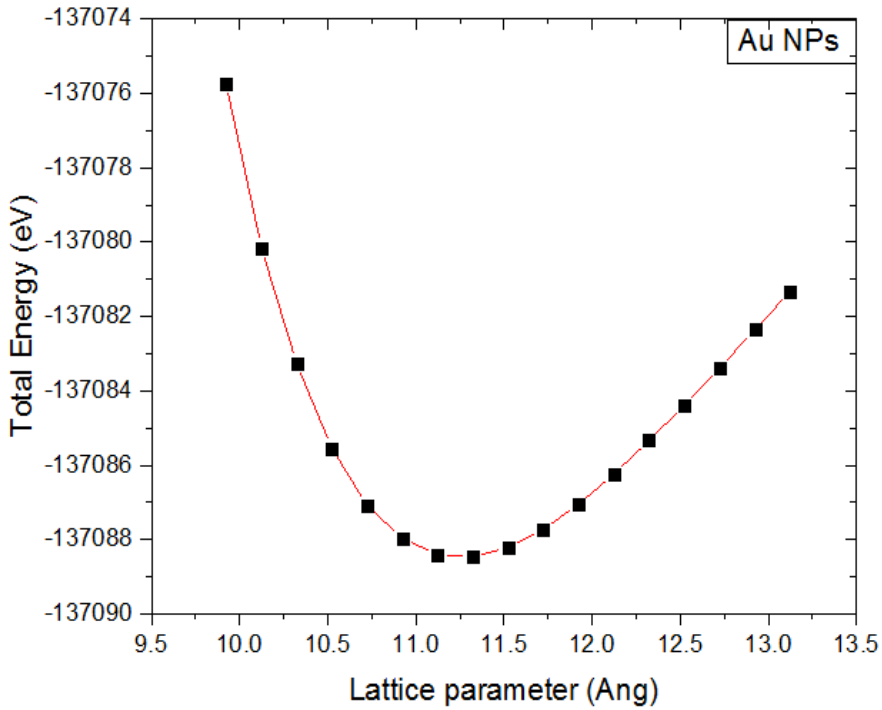

Figure 4.1 : The calculated energy VS. Lattice parameter curves for optimizing the lattice constants as (a_{Au}) NPs

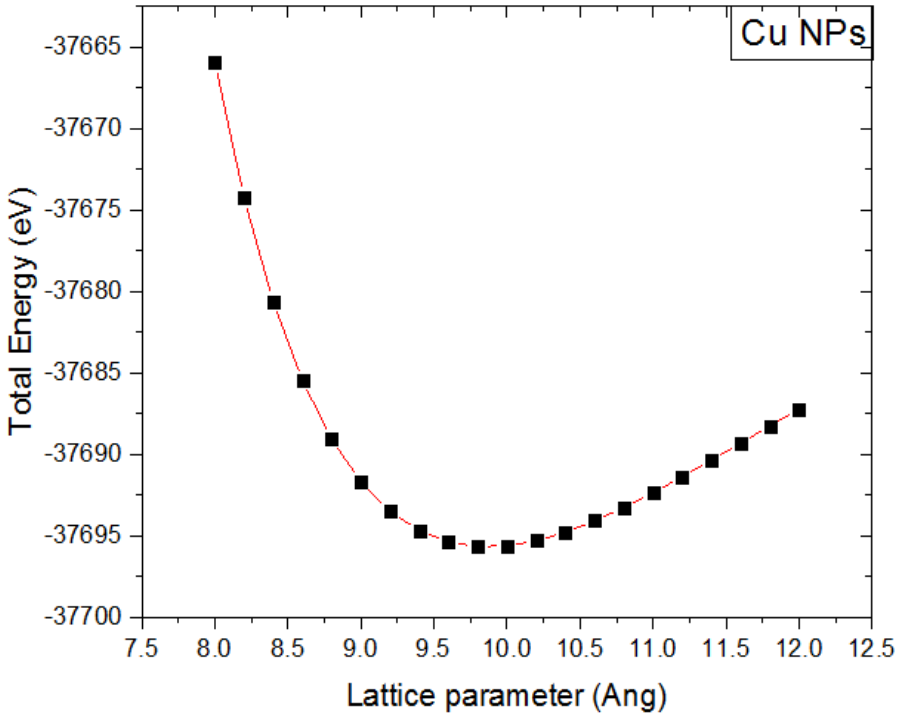

Figure 4.2: The calculated energy vs lattice parameter curves for optimizing the lattice constants as (a_{Cu}) NPs.

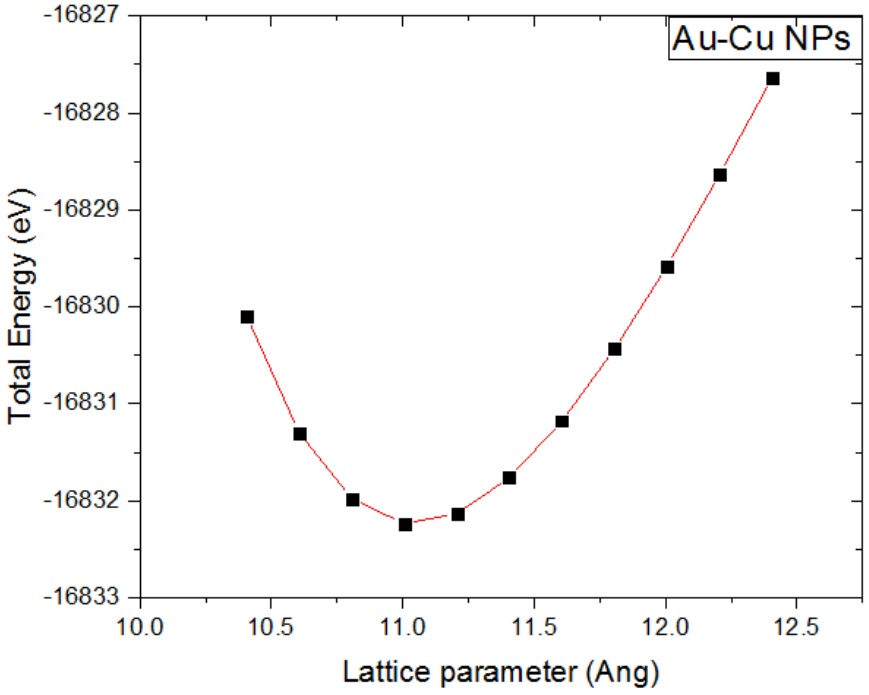

Figure 4.3: The calculated energy VS. Lattice parameter curves for optimizing the lattice constants as a_{Au-Cu}) NPs.

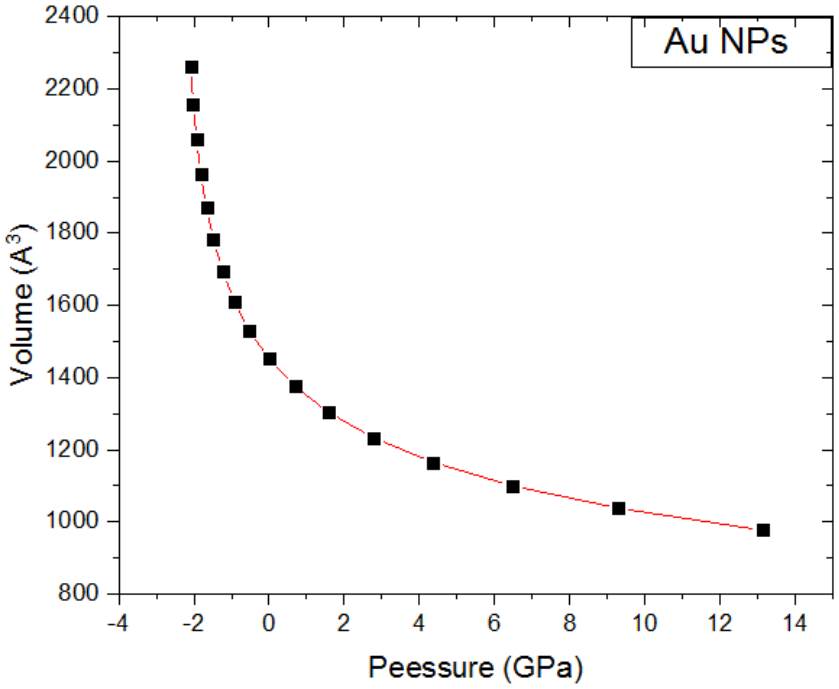

Figure 1.4 Compression data of (Au) NPs. at zero temperature. The solid curve is a least squares fit of the first-principles calculations data

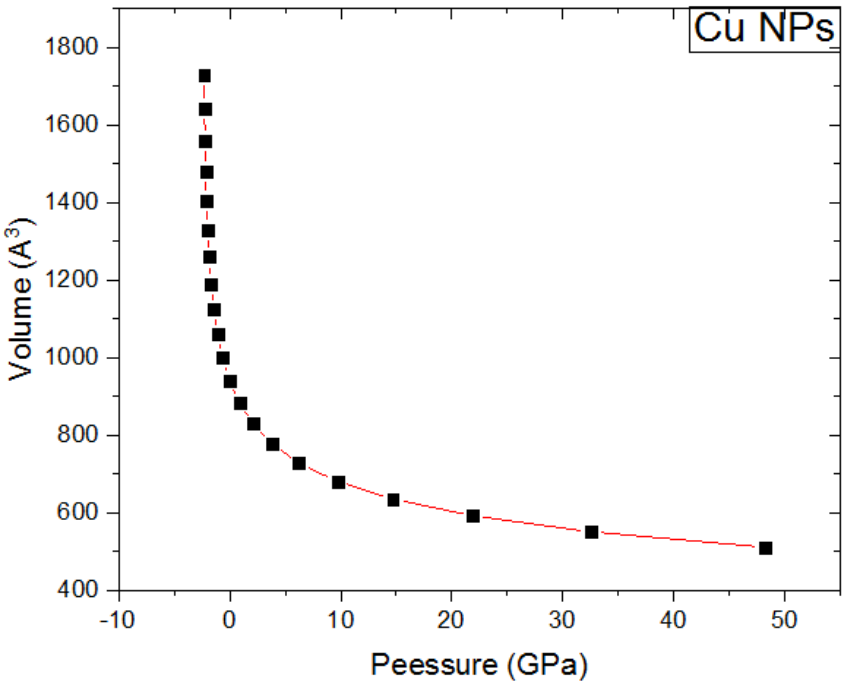

Figure 4.5: Compression data of Cu NPs at zero temperature. The solid curve is a least squares fit of the first-principles calculations data

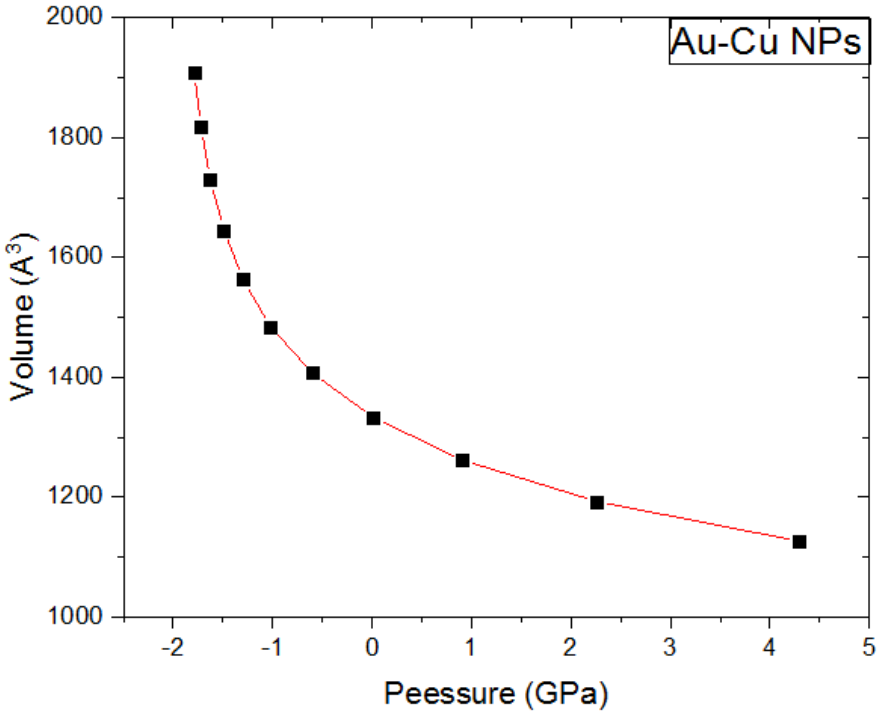

Figure 4.6: Compression data of (Au-Cu) NPs at zero temperature. The solid curve is a least squares fit of the first-principles calculations data

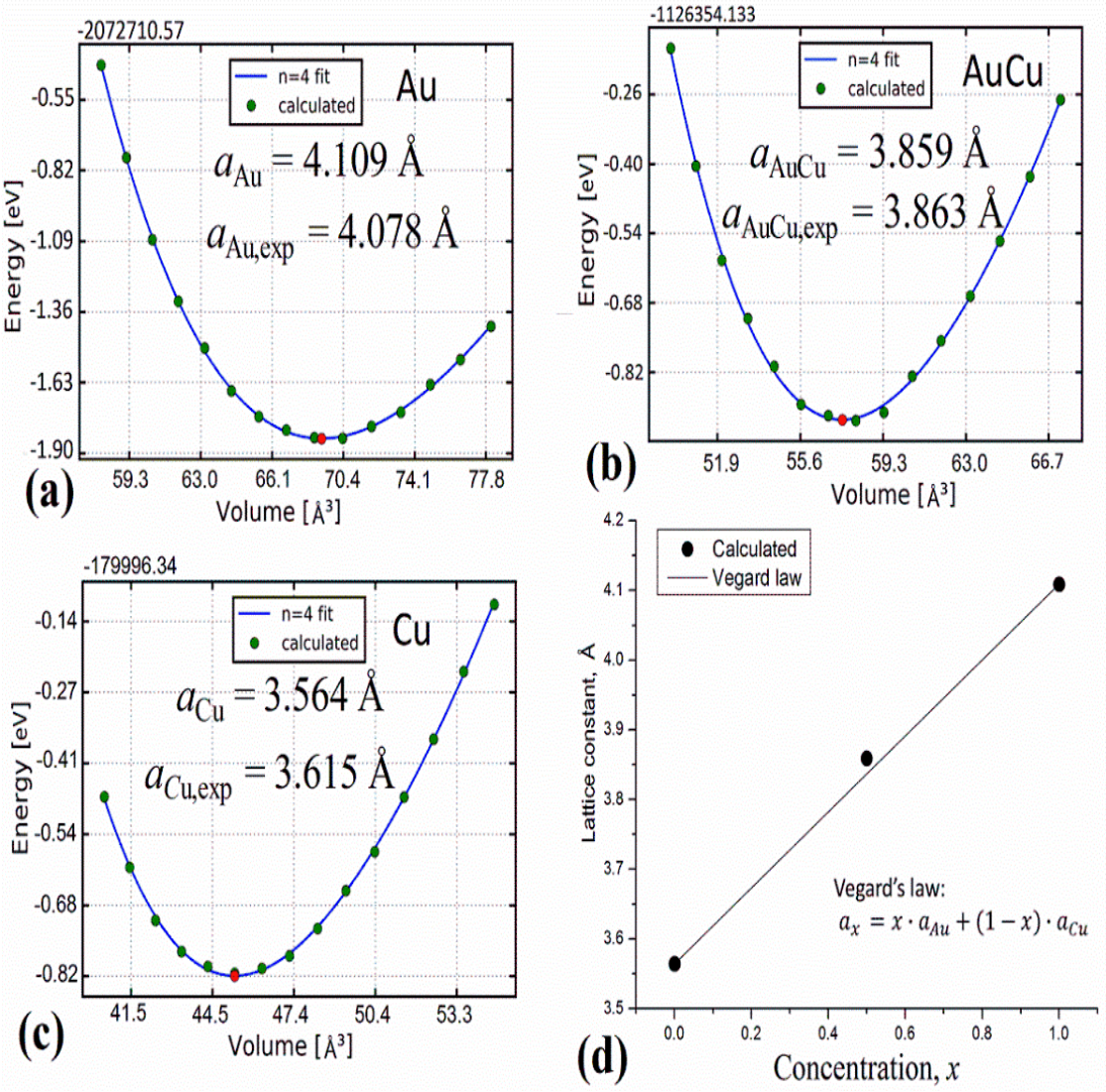

Figure 4.7: The calculated Energy vs. Volume curves for optimizing the lattice constants as a_{Au}, a_{AuCu} and a_{Cu}, respectively, for (a) Au (b) AuCu with and (c) Cu bulk structures. (d) Fitting the optimized lattice constants (black squares) in (a)-(c) to Vegard law (solid line). Notice, the experimental lattice constants written beneath the optimized ones in (a) – (c).

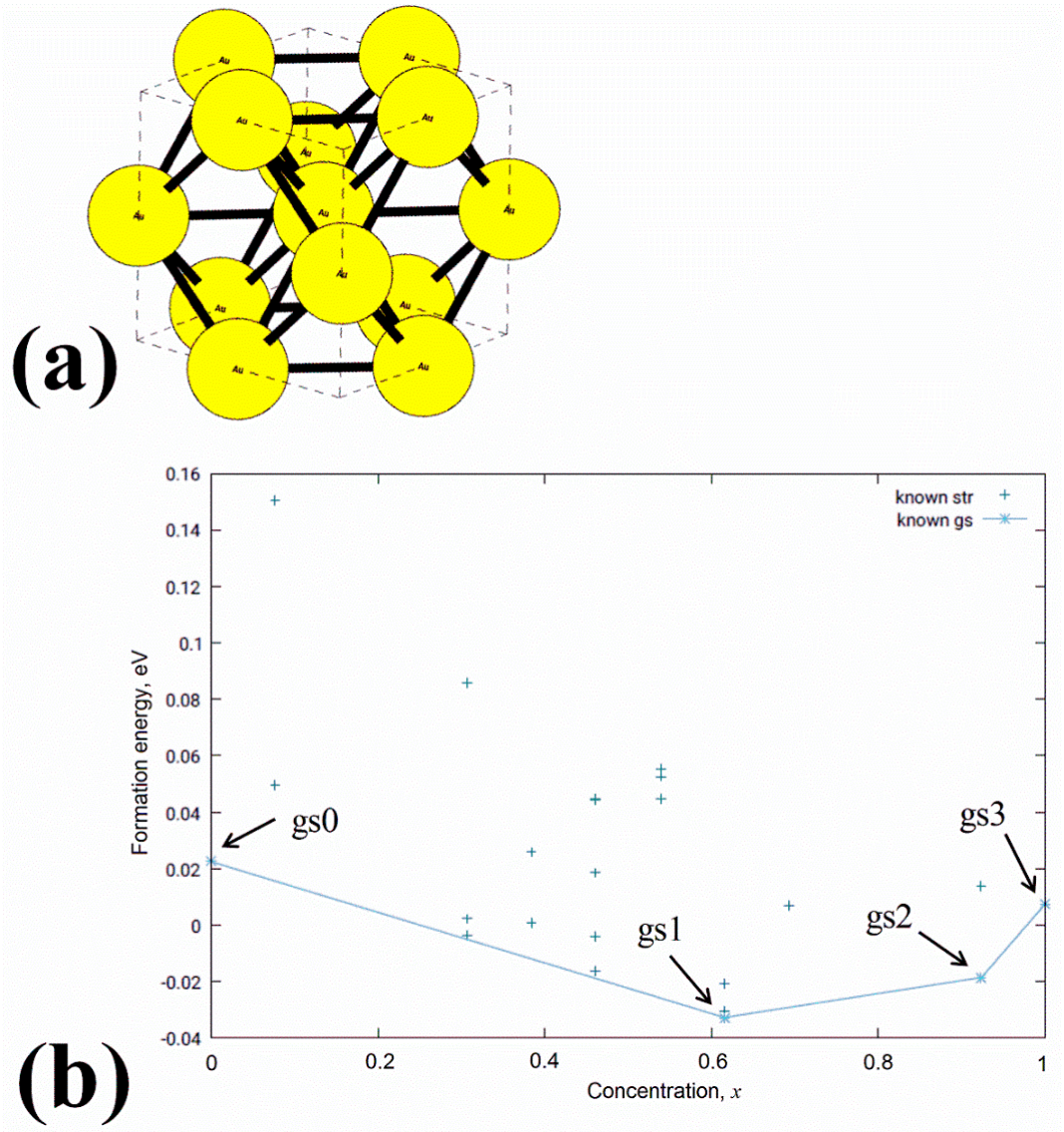

Figure 4.8: (a) Au nanoparticle with 13 Au atoms generated with ASE program using the Wulff-construction method. (b) The structure formation energy versus the structure concentration produced by the maps program. Among known structures (shown as crosses) the ground state structures gs0 – gs3 are the ones that reside on the convex hull (solid line).

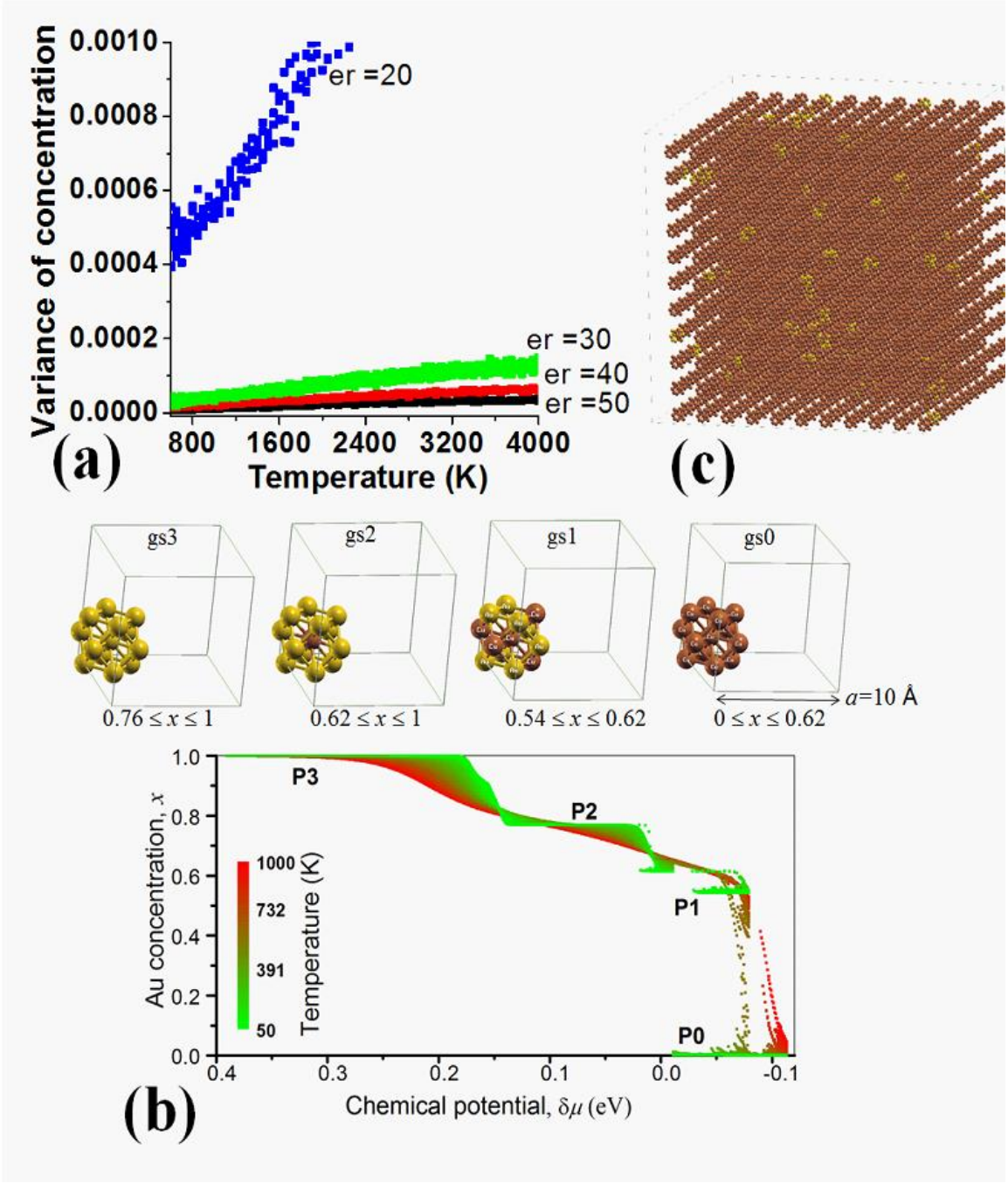

Figure 4.9: (a) Monte Carlo simulation convergence test for the size (er) of the simulation cell (b) Phase diagram of Au_xCu_{1-x} Nano-alloys. Insets: structures of the Nano-alloys (each with 13 atoms) for the calculated stable ground states gs0 – gs3. These Nano-alloys are placed in empty boxes with sides ~ "*a*". (c) An example of a monte-carlo simulation super-cell consisting of periodic arrangements of structures associated with a give ground-state.

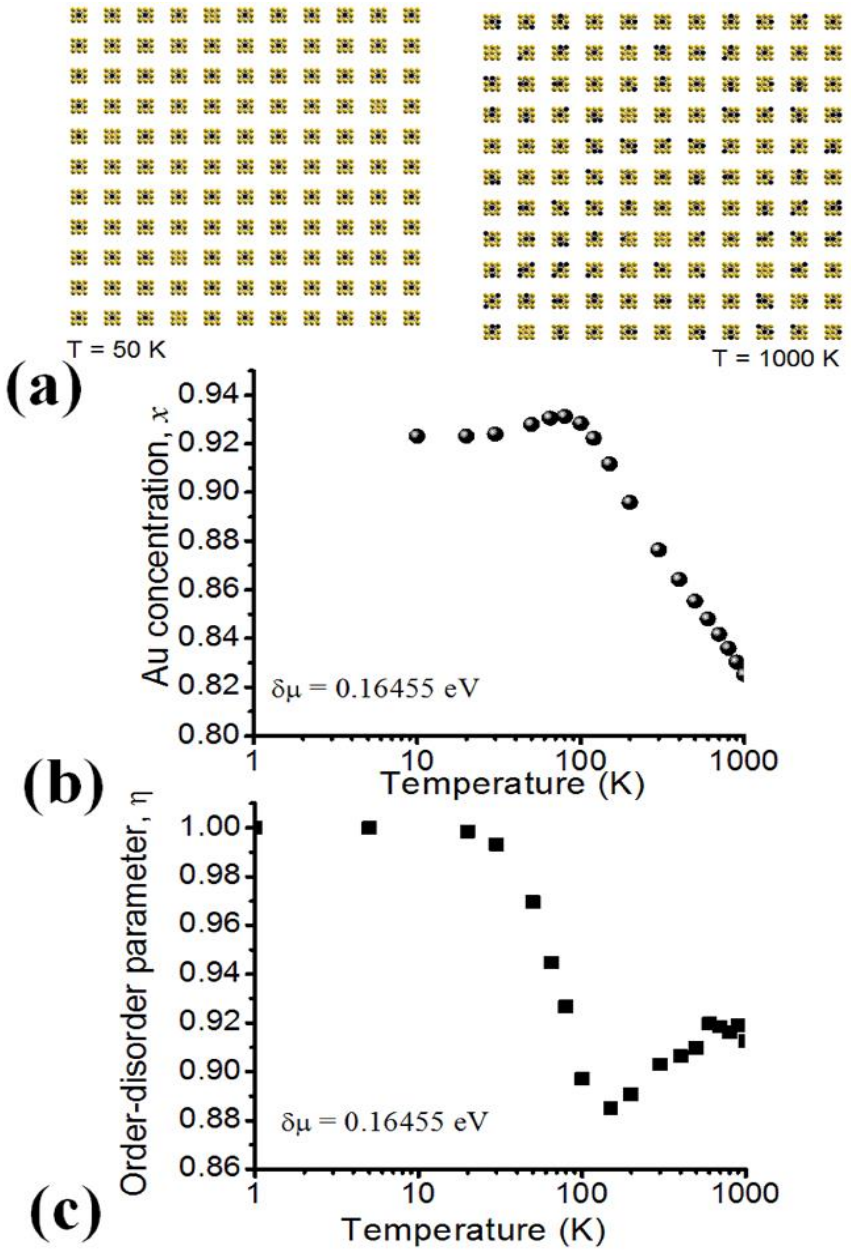

Figure 4.10: (a) snap shot of the cross-sectional region of the Monte-Carlo simulation cell at 50 K (left snapshot) and 1000 K (right snapshot), clearly indicating the ordered and disordered distribution of the Cu (black circles) among the Nano-alloys at low and high temperatures, respectively. The bright circles are the Au atoms. (b) The concentration, *x*, versus the temperature at the chemical potential $\delta\mu = 0.16455$ eV corresponding to the stable ground state 2 (gs2). (c) The order parameter as a function of temperature for gs2 at $\delta\mu = 0.16466$ eV.

4.1.3 Discussion

The results are shown in Figure (4.1 ,4.2, and 4.3) The equilibrium lattice parameter was found using the GGA functional. The calculated results for equilibrium lattice are summarized in the (Table 4.1). . The bulk modulus K_0 was determined from the results of total energy change with respect to the hydrostatic variation of volume and fitted to the fourth-order Birch-Murnaghan equation of state. These results in bulk modulus as summarized in the Table 4.1.

The Monte-Carlo code (emc2) performed the calculations in a cell consisting of 11×11×11 (i.e. super-cell) structures associated with the respective ground state of interest. Figure 4.9 (c) shows an example of such a super-cell. Therefore, the concentration *x* in Figure 4.9 (b) corresponds to the average concentration over the entire super-cell. It is very important to emphasis here that our results in Figure 4.9 (b) are related to a large ensemble of non-interacting Nano-alloys (i.e each $Au_{1-x}Cu_x$ Nano-alloy consists of 13 atoms). This is because the super-cell was consisting of isolated Nano-alloys separated from each other by a vacuum box with size $a \sim 10$ Å (see right inset of Figure 4.9 (b).

Therefore, adding Au or Cu atoms to a Nano-alloy occurs in a discrete manner, leading to the observed discrete jumps between the plateaus of stable *x* at $T < 100$ K. This is analogues to the case of discrete charging of a nano-device (e.g. a quantum dot), connected to electron reservoir terminals, which occurs one electron at a time whenever the reservoir's electro-chemical potential (or Fermi level) aligns with the narrow electro-chemical potential of the nano-device, leading to the stair-case pattern (plateaus) in the plane of the nano-device current versus the bias voltage.

However, as *T* increases, the plateaus gradually smear out as shown in Fig. 4.9 (b) at $T \sim 1000$ K (Red region). This smearing out can simply be

attributed to the temperature broadening of $\delta\mu$, allowing for the ground states with similar space-groups (e.g. g s0, gs2, and gs3 are having m3-m space group symmetry) to coalesce at higher temperatures. That could explain why structures belonging to gs1 (having 4_2m symmetry, i.e. tetragonal based on atomic arrangement) were confined to $T < 300$ K (A careful look at Figure 4.9 (b) around $0.54 \leq x \leq 0.62$ would reveal this confinement).

We have also observed that the low-to-high temperature transition in Figure 4.9 (b) was accompanied by order-to-disorder transition as shown in Figure 4.10 (a), where the left panel shows a cross-section view of the Monte-Carlo (emc2) simulation cell belonging to gs2 (namely at $x = 0.62$) at 50 K with ordered atomic arrangements such that each Cu (dark sphere) is symmetrically surrounded by 12 Au atoms (golden spheres). The disordered arrangement at 1000 K can clearly be viewed in the right panel. Figure 4.10 (b) shows that, for gs2, x is almost fixed for $T < 100$ K then decreases after 100K. The region with nearly constant x are associated with the ordered phase. As T increases addition of more Cu atoms becomes favorable, enhancing the disordered phase.

4.2 Conclusions

We have calculated the phase structure (chemical potential versus concentration with the temperature as a parameter) of $Au_{1-x}Cu_x$ nanoparticle (or Nano-alloy) from a combination of first-principle and Monte-Carlo methods. Plateau patterns, associated with the calculated configurational ,ground states have been observed at low temperatures < 100 K. The plateaus smeared out at higher temperatures, giving rise to the order-disorder transitions with temperature. The critical temperature for this

transition was estimated at 100 K, consistent with the reported trend of the transition temperature with the Nano alloy size.

4.3 Recommendation

From here, future work can take many possible avenues for the phase transition study in Gold-Copper Nano alloys, there is a natural place to continue; now that we know the phase transition, we can start looking for suitable dopants to study their optical and electronic properties by First Principle and Monte-Carlo Calculations for a larger number of atoms

Reference

[1] R. He, Y.-C. Wang, X. Wang, Z. Wang, G. Liu, W. Zhou, L. Wen, Q. Li, X. Wang, X. Chen, Facile synthesis of pentacle gold–copper alloy nanocrystals and their plasmonic and catalytic properties, Nature communications 5 (2014) 4327.

[2] P. Fedorov, S. Volkov, Au–Cu Phase Diagram, Russian Journal of Inorganic Chemistry 61 (2016) 772-775.

[3] C. Powell, H. Michels, Copper-Nickel for Seawater Corrosion Resistance and Antifouling: A State of the Art Review, Rem 90 (2000) 10.

[4] S.-H. Wei, A. Mbaye, L. Ferreira, A. Zunger, First-principles calculations of the phase diagrams of noble metals: Cu-Au, Cu-Ag, and Ag-Au, Physical Review B 36 (1987) 4163.

[5] X. Teng, Q. Wang, P. Liu, W. Han, A.I. Frenkel, W. Wen, N. Marinkovic, J.C. Hanson, J.A. Rodriguez, Formation of Pd/Au nanostructures from Pd nanowires via galvanic replacement reaction, Journal of the American Chemical Society 130 (2008) 1093-1101.

[6] R. Ferrando, J. Jellinek, R.L. Johnston, Nanoalloys: from theory to applications of alloy clusters and nanoparticles, Chemical reviews 108 (2008) 845-910.

[7] M. Brust, M. Walker, D. Bethell, D.J. Schiffrin, R. Whyman, Synthesis of thiol-derivatised gold nanoparticles in a two-phase liquid–liquid system, Journal of the Chemical Society, Chemical Communications (1994) 801-802.

[8] F. Baletto, R. Ferrando, Structural properties of nanoclusters: Energetic, thermodynamic, and kinetic effects, Reviews of modern physics 77 (2005) 371.

[9] G. Bozzolo, J. Ferrante, R.D. Noebe, B. Good, F.S. Honecy, P. Abel, Surface segregation in multicomponent systems: Modeling of surface alloys and alloy surfaces, Computational materials science 15 (1999) 169-195.

[10] R. Pacheco-Contreras, J.O. Juárez-Sánchez, M. Dessens-Félix, F. Aguilera-Granja, A. Fortunelli, A. Posada-Amarillas, Empirical-potential global minima and DFT local minima of trimetallic AglAumPtn (l+m+n= 13, 19, 33, 38) clusters, Computational Materials Science 141 (2018) 30-40.

[11] M.P. Andrews, S.C. O'Brien, Gas-phase" molecular alloys" of bulk immiscible elements: iron-silver (FexAgy), The Journal of Physical Chemistry 96 (1992) 8233-8241.

[12] M.S. Bailey, N.T. Wilson, C. Roberts, R.L. Johnston, Structures, stabilities and ordering in Ni-Al nanoalloy clusters, The European Physical Journal D - Atomic, Molecular, Optical and Plasma Physics 25 (2003) 41-55.

[13] N.T. Wilson, R.L. Johnston, A theoretical study of atom ordering in copper–gold nanoalloy clusters, Journal of Materials Chemistry 12 (2002) 2913-2922.

[14] M. Bailey, N. Wilson, C. Roberts, R. Johnston, Structures, stabilities and ordering in Ni-Al nanoalloy clusters, The European Physical Journal D-Atomic, Molecular, Optical and Plasma Physics 25 (2003) 41-55.

[15] W.B. Pearson, Crystal chemistry and physics of metals and alloys, (1972).

[16] P.P. Edwards, J.M. Thomas, Gold in a Metallic Divided State—From Faraday to Present‐Day Nanoscience, Angewandte Chemie International Edition 46 (2007) 5480-5486.

[17] T.W. Odom, C.L. Nehl, How Gold Nanoparticles Have Stayed in the Light: The 3M's Principle, ACS nano 2 (2008) 612-616.
[18] N.E. Motl, Synthesis and Applications of Gold and Gold-copper Alloy Nanoparticles, (2012).
[19] S.A. Maier, M.L. Brongersma, P.G. Kik, S. Meltzer, A.A. Requicha, H.A. Atwater, Plasmonics—a route to nanoscale optical devices, Advanced materials 13 (2001) 1501-1505.
[20] Y. Alivov, Z. Fan, Efficiency of dye sensitized solar cells based on TiO 2 nanotubes filled with nanoparticles, Applied Physics Letters 95 (2009) 063504.
[21] K. Kneipp, Y. Wang, H. Kneipp, L.T. Perelman, I. Itzkan, R.R. Dasari, M.S. Feld, Single molecule detection using surface-enhanced Raman scattering (SERS), Physical review letters 78 (1997) 1667.
[22] S. Lal, N.K. Grady, J. Kundu, C.S. Levin, J.B. Lassiter, N.J. Halas, Tailoring plasmonic substrates for surface enhanced spectroscopies, Chemical Society Reviews 37 (2008) 898-911.
[23] W. Hasan, C.L. Stender, M.H. Lee, C.L. Nehl, J. Lee, Tailoring the structure of nanopyramids for optimal heat generation, Nano letters 9 (2009) 1555-1558.
[24] S. Link, M.A. El-Sayed, Spectral properties and relaxation dynamics of surface plasmon electronic oscillations in gold and silver nanodots and nanorods, ACS Publications, 1999.
[25] N.E. Motl, E. Ewusi-Annan, I.T. Sines, L. Jensen, R.E. Schaak, Au−Cu alloy nanoparticles with tunable compositions and plasmonic properties: experimental determination of composition and correlation with theory, The Journal of Physical Chemistry C 114 (2010) 19263-19269.

[26] H. Landolt, R. Börnstein, Phase equilibria, crystallographic and thermodynamic data of binary alloys, Springer-Verlag1993.
[27] J.M. Prausnitz, R.N. Lichtenthaler, E.G. de Azevedo, Molecular thermodynamics of fluid-phase equilibria, Pearson Education1998.
[28] H. Zhang, J.F. Banfield, Understanding polymorphic phase transformation behavior during growth of nanocrystalline aggregates: insights from TiO2, The Journal of Physical Chemistry B 104 (2000) 3481-3487.
[29] W. Greiner, L. Neise, H. Stöcker, Thermodynamics and statistical mechanics, Springer Science & Business Media2012.
[30] D.R. Olander, A.T. Motta, A new book:'light-water reactor materials', Nuclear Engineering and Technology 37 (2005) 309-316.
[31] D.A. Porter, K.E. Easterling, M. Sherif, Phase Transformations in Metals and Alloys, (Revised Reprint), CRC press2009.
[32] M. Butt, Study of gold-based alloy phase diagrams, Brunel University School of Engineering and Design PhD Theses, 1990.
[33] W.G. McMillan Jr, J.E. Mayer, The statistical thermodynamics of multicomponent systems, The Journal of Chemical Physics 13 (1945) 276-305.
[34] C.J. Adkins, Equilibrium thermodynamics, Cambridge University Press1983.
[35] I. Dincer, Y.A. Cengel, Energy, entropy and exergy concepts and their roles in thermal engineering, Entropy 3 (2001) 116-149.
[36] Y. Fukai, The structure and phase diagram of M–H systems at high chemical potentials—High pressure and electrochemical synthesis, Journal of alloys and compounds 404 (2005) 7-15.
[37] M.D. Tissandier, K.A. Cowen, W.Y. Feng, E. Gundlach, M.H. Cohen, A.D. Earhart, J.V. Coe, T.R. Tuttle, The proton's absolute aqueous

enthalpy and Gibbs free energy of solvation from cluster-ion solvation data, The Journal of Physical Chemistry A 102 (1998) 7787-7794.
[38] D. Kondepudi, I. Prigogine, Modern thermodynamics: from heat engines to dissipative structures, John Wiley & Sons2014.
[39] A. Bejan, Entropy generation minimization: The new thermodynamics of finite‐size devices and finite‐time processes, Journal of Applied Physics 79 (1996) 1191-1218.
[40] P. Bombarda, C.M. Invernizzi, C. Pietra, Heat recovery from Diesel engines: A thermodynamic comparison between Kalina and ORC cycles, Applied Thermal Engineering 30 (2010) 212-219.
[41] Y.A. Cengel, R.H. Turner, J.M. Cimbala, M. Kanoglu, Fundamentals of thermal-fluid sciences, McGraw-Hill New York2008.
[42] W.A.F. Mohamed, PVT Lab Manual.
[43] I. Levine, N (1978).", Physical Chemistry" University of Brooklyn: McGraw-Hill.
[44] S. Chien-Min, R.G. Burns, Kinetics of high-pressure phase transformations: implications to the evolution of the olivine→ spinel transition in the downgoing lithosphere and its consequences on the dynamics of the mantle, Tectonophysics 31 (1976) 1-32.
[45] A. Lavakumar, Concepts in Physical Metallurgy.
[46] G. INDEN, Equilibrium Phase Diagrams, (2007).
[47] L.K. Reddy, Principles of engineering metallurgy, New Age International2007.
[48] W.D. Callister Jr, D.G. Rethwisch, Fundamentals of materials science and engineering: an integrated approach, John Wiley & Sons2012.
[49] A. Mostafa, M. Medraj, Binary Phase Diagrams and Thermodynamic Properties of Silicon and Essential Doping Elements (Al, As, B, Bi, Ga, In, N, P, Sb and Tl), Materials 10 (2017) 676.

[50] J.-C. Zhao, Methods for phase diagram determination, elsevier2011.
[51] J. Ågren, A thermodynamic analysis of the Fe− C and Fe− N phase diagrams, Metallurgical Transactions A 10 (1979) 1847-1852.
[52] D.O.a.A. Motta, Light Water Reactor Materials, 2018.
[53] P. Spencer, A brief history of CALPHAD, Calphad 32 (2008) 1-8.
[54] S. Abdessameud, Thermodynamic Modeling of the Mg-Al-Li-Na-H System for Solid State Hydrogen Storage Applications, Concordia University, 2016.
[55] A. Pribram-Jones, D.A. Gross, K. Burke, Dft: A theory full of holes?, Annual review of physical chemistry 66 (2015) 283-304.
[56] J.C. Cuevas, Introduction to density functional theory, Universität Karlsruhe, Germany (2010).
[57] D.J. Auerbach, A.M. Wodtke, Vibrational Energy Transfer at Surfaces: The Importance of Non-Adiabatic Electronic Effects, in: R. Díez Muiño, H.F. Busnengo (Eds.), Dynamics of Gas-Surface Interactions: Atomic-level Understanding of Scattering Processes at Surfaces, Springer Berlin Heidelberg, Berlin, Heidelberg, 2013, pp. 267-297.
[58] A. Kakekhani, Using Ferroelectrics to Tackle Fundamental Challenges in Catalysis, Yale University2016.
[59] J.P. Perdew, K. Burke, M. Ernzerhof, Generalized gradient approximation made simple, Physical review letters 77 (1996) 3865.
[60] M. Cui, H. Lu, H. Jiang, Z. Cao, X. Meng, Phase diagram of continuous binary nanoalloys: size, shape, and segregation effects, Scientific Reports 7 (2017) 41990.
[61] F. Berthier, E. Maras, B. Legrand, Phase diagrams of nanoalloys: influence of size and morphology, Physical Chemistry Chemical Physics 17 (2015) 28347-28353.

[62] R. Mendoza-Cruz, L. Bazán-Diaz, J. Velázquez-Salazar, J. Samaniego-Benitez, F. Ascencio-Aguirre, R. Herrera-Becerra, M. José-Yacamán, G. Guisbiers, Order–disorder phase transitions in Au–Cu nanocubes: from nano-thermodynamics to synthesis, Nanoscale 9 (2017) 9267-9274.
[63] D.A. Drabold, S.K. Estreicher, Defect theory: An armchair history, Theory of Defects in Semiconductors, Springer2007, pp. 11-28.
[64] A. van de Walle, The Alloy-Theoretic Automated Toolkit (ATAT): A User Guide, (2010).
[65] A. van de Walle, G. Ceder, Automating first-principles phase diagram calculations, Journal of Phase Equilibria 23 (2002) 348.
[66] A.R. Denton, N.W. Ashcroft, Vegard's law, Physical review A 43 (1991) 3161.
[67] R. Abe, Giant cluster expansion theory and its application to high temperature plasma, Progress of Theoretical Physics 22 (1959) 213-226.
[68] A. Van de Walle, M. Asta, Self-driven lattice-model Monte Carlo simulations of alloy thermodynamic properties and phase diagrams, Modelling and Simulation in Materials Science and Engineering 10 (2002) 521.
[69] F. Calvo, Thermodynamics of nanoalloys, Physical Chemistry Chemical Physics 17 (2015) 27922-27939.
[70] W. Soffa, D.E. Laughlin, Diffusional phase transformations in the solid state, Physical Metallurgy (Fifth Edition), Elsevier2015, pp. 851-1020.

Appendices

Appendix A:

1. Example of elk input file

tasks
1

swidth
0.05

avec
21.77604010 0.00000000 0.00000000
0.00000000 21.77604010 0.00000000
0.00000000 0.00000000 21.77604010

sppath
'/home/mahk/Programs/elk-4.3.6/species/'

atoms
1
'Au.in'
13
1

nempty
30

rgkmax
7.0

ngridk

4 4 4

2. Command running of elk code

elk

3.example of elk Output file

```
+----------------------------+
| Elk version 4.3.06 started |
+----------------------------+

Date (YYYY-MM-DD) : 2017-08-30
Time (hh:mm:ss)   : 09:05:18

All units are atomic (Hartree, Bohr, etc.)

+-----------------------------------------------+
| Ground-state run starting from atomic densities |
+-----------------------------------------------+

Lattice vectors :
  0.000000000   0.000000000  -20.22593246
  0.000000000  -20.22593246    0.000000000
 -20.22593246   0.000000000   0.000000000

Reciprocal lattice vectors :
 -0.000000000  -0.000000000  -0.3106499698
 -0.000000000  -0.3106499698  -0.000000000
```

-0.3106499698 -0.000000000 -0.000000000

Unit cell volume : 8274.193213
Brillouin zone volume : 0.2997877945E-01

Species : 1 (Au)
parameters loaded from : Au.in
name : gold
nuclear charge : -79.00000000
electronic charge : 79.00000000
atomic mass : 359048.0559
muffin-tin radius : 2.523325775
number of radial points in muffin-tin : 697
number on inner part of muffin-tin : 497
atomic positions (lattice), magnetic fields (Cartesian) :
1 : 0.00000000 0.00000000 0.00000000 0.00000000 0.00000000 0.00000000
2 : 0.17818100 0.82181900 0.00000000 0.00000000 0.00000000 0.00000000
3 : 0.82181800 0.82181900 0.00000000 0.00000000 0.00000000 0.00000000
4 : 0.00000000 0.64363700 0.00000000 0.00000000 0.00000000 0.00000000
5 : 0.17818100 0.00000000 0.82181900 0.00000000 0.00000000 0.00000000
6 : 0.82181800 0.00000000 0.82181900 0.00000000 0.00000000 0.00000000

Species : 2 (Cu)
parameters loaded from : Cu.in
name : copper
nuclear charge : -29.00000000
electronic charge : 29.00000000

atomic mass : 115837.2717
muffin-tin radius : 2.400000000
number of radial points in muffin-tin : 497
number on inner part of muffin-tin : 349
atomic positions (lattice), magnetic fields (Cartesian) :
1 : 0.00000000 0.00000000 0.64363700 0.00000000 0.00000000 0.00000000
2 : 0.17818100 0.64363700 0.82181900 0.00000000 0.00000000 0.00000000
3 : 0.17818100 0.82181900 0.64363700 0.00000000 0.00000000 0.00000000
4 : 0.00000000 0.82181900 0.82181900 0.00000000 0.00000000 0.00000000
5 : 0.82181800 0.64363700 0.82181900 0.00000000 0.00000000 0.00000000
6 : 0.82181800 0.82181900 0.64363700 0.00000000 0.00000000 0.00000000
7 : 0.00000000 0.64363700 0.64363700 0.00000000 0.00000000 0.00000000

Total number of atoms per unit cell : 13

Spin treatment :
spin-unpolarised

Number of Bravais lattice symmetries : 48
Number of crystal symmetries : 2
Crystal has no inversion symmetry
Complex Hermitian eigensolver will be used

k-point grid : 2 2 2
k-point offset : 0.000000000 0.000000000 0.000000000
k-point set is reduced with full crystal symmetry group

Total number of k-points : 8

Muffin-tin radius times maximum |G+k| : 7.000000000
using average radius
Maximum |G+k| for APW functions : 2.849096093
Maximum (1/2)|G+k|^2 : 4.058674274
Maximum |G| for potential and density : 12.00000000
Constant for pseudocharge density : 8
Radial integration step length : 4

G-vector grid sizes : 80 80 80
Number of G-vectors : 241497

Maximum angular momentum used for
APW functions : 8
H and O matrix elements outer loop : 7
outer part of muffin-tin : 7
inner part of muffin-tin : 3

Total nuclear charge : -677.0000000
Total core charge : 372.0000000
Total valence charge : 305.0000000
Total excess charge : 0.000000000
Total electronic charge : 677.0000000

Effective Wigner radius, r_s : 1.428947019

Number of empty states : 390
Total number of valence states : 543
Total number of core states : 372

Total number of local-orbitals : 305

Exchange-correlation functional : 22 0 0
PBEsol, Phys. Rev. Lett. 100, 136406 (2008)
Generalised gradient approximation (GGA)

Smearing type : 3
Fermi-Dirac
Smearing width : 0.5000000000E-01
Effective electronic temperature (K) : 15788.75213

Mixing type : 1
Adaptive linear mixing

Density and potential initialised from atomic data

+-----------------------------+
| Self-consistent loop started |
+-----------------------------+

+--------------------+
| Loop number : 1 |
+--------------------+

Energies :
Fermi : -0.630279770113E-01
sum of eigenvalues : -77136.4472818
electron kinetic : 143231.777796
core electron kinetic : 136463.711921
Coulomb : -266138.579362
Coulomb potential : -216930.127234
nuclear-nuclear : 2873.19559646
electron-nuclear : -321093.422683
Hartree : 52081.6477246
Madelung : -157673.515745

xc potential : -3438.09784334
exchange : -2569.07998895
correlation : -43.2265077135
electron entropic : -3.27638264585
total energy : -125522.384446

Density of states at Fermi energy : 378.5400736
(states/Hartree/unit cell)

Estimated indirect band gap : 0.1586458807E-01
from k-point 8 to k-point 8
Estimated direct band gap : 0.1586458807E-01
at k-point 8

Charges :
core : 372.0000000
valence : 305.0000000
interstitial : 23.25639305
muffin-tins (core leakage)
species : 1 (Au)
atom 1 : 77.47209295 (0.4461285372E-03)
atom 2 : 77.45326290 (0.4444486186E-03)
atom 3 : 77.45326290 (0.4444486186E-03)
atom 4 : 77.43631453 (0.4426993341E-03)
atom 5 : 77.43368436 (0.4426710881E-03)
atom 6 : 77.43368436 (0.4426710881E-03)
species : 2 (Cu)
atom 1 : 26.92952970 (0.1633255642E-03)
atom 2 : 26.92772907 (0.1632792937E-03)
atom 3 : 26.90614768 (0.1626610145E-03)
atom 4 : 27.57861860 (0.1745843174E-03)
atom 5 : 26.92772907 (0.1632792937E-03)
atom 6 : 26.90614768 (0.1626610145E-03)

```
  atom    7               :    26.88540315     (  0.1619902596E-03)
 total in muffin-tins       :    653.7436069
 total calculated charge    :    676.9141596
 total charge               :    677.0000000
 error                      :   0.8584037229E-01

Time (CPU seconds) :      4026.74

+--------------------------+
| Elk version 4.3.06 stopped |
+--------------------------+
```

Appendix B:

1. Example of Quantum-Espresso input file

```
&CONTROL
  calculation = "scf",
  pseudo_dir  = "/home/mujahid/Downloads/espresso-4.3.2/pseudo",
  outdir      = "/home/mujahid/Downloads/espresso-4.3.2/tmp",
/
&SYSTEM
  ibrav       = 0,
A=11.00800
  nat         = 13,
  ntyp        = 2,
  ecutwfc     = 40.D0,
  occupations = "smearing",
  smearing    = "methfessel-paxton",
  degauss     = 0.05D0,
/
&ELECTRONS
```

```
  conv_thr    = 1.D-6,
  mixing_beta = 0.3D0,
/
ATOMIC_SPECIES
Au  1.0  Au.pbe-dn-rrkjus_psl.0.1.UPF
Cu  1.0  Cu.pbe-kjpaw.UPF
K_POINTS automatic
2 2 2 0 0 0
CELL_PARAMETERS alat
    0.00000000   0.00000000  -1.00000000
    0.00000000  -1.00000000   0.00000000
   -1.00000000   0.00000000   0.00000000
```

2. Command running

ev,x

3. Example of Quantum-Espresso Output file

```
    Program PWSCF v.6.2 starts on  9Apr2018 at  2:35: 7

    This program is part of the open-source Quantum ESPRESSO suite
    for quantum simulation of materials; please cite
        "P. Giannozzi et al., J. Phys.:Condens. Matter 21 395502 (2009);
        "P. Giannozzi et al., J. Phys.:Condens. Matter 29 465901 (2017);
         URL http://www.quantum-espresso.org",
    in publications or presentations arising from this work. More details at
    http://www.quantum-espresso.org/quote

    Serial version
```

Waiting for input...
Reading input from standard input
Message from routine read_cards :
DEPRECATED: no units specified in ATOMIC_POSITIONS card
Message from routine read_cards :
ATOMIC_POSITIONS: units set to alat

Current dimensions of program PWSCF are:
Max number of different atomic species (ntypx) = 10
Max number of k-points (npk) = 40000
Max angular momentum in pseudopotentials (lmaxx) = 3
file Au.pbe-dn-rrkjus_psl.0.1.UPF: wavefunction(s) 5D renormalized

G-vector sticks info
---
sticks: dense smooth PW G-vecs: dense smooth PW
Sum 5917 5917 1605 342243 342243 48297

bravais-lattice index = 0
lattice parameter (alat) = 21.5546 a.u.
unit-cell volume = 10014.2809 (a.u.)^3
number of atoms/cell = 13
number of atomic types = 2
number of electrons = 143.00
number of Kohn-Sham states= 86
kinetic-energy cutoff = 40.0000 Ry
charge density cutoff = 160.0000 Ry
convergence threshold = 1.0E-06
mixing beta = 0.3000
number of iterations used = 8 plain mixing
Exchange-correlation = SLA PW PBX PBC (1 4 3 4 0 0)

celldm(1)= 21.554598 celldm(2)= 0.000000 celldm(3)= 0.000000
celldm(4)= 0.000000 celldm(5)= 0.000000 celldm(6)= 0.000000

crystal axes: (cart. coord. in units of alat)

a(1) = (0.000000 0.000000 -1.000000)

a(2) = (0.000000 -1.000000 0.000000)

a(3) = (-1.000000 0.000000 0.000000)

reciprocal axes: (cart. coord. in units 2 pi/alat)

b(1) = (0.000000 0.000000 -1.000000)

b(2) = (0.000000 -1.000000 0.000000)

b(3) = (-1.000000 0.000000 0.000000)

PseudoPot. # 1 for Au read from file:

/home/mujahid/Downloads/espresso-4.3.2/pseudo/Au.pbe-dn-rrkjus_psl.0.1.UPF

MD5 check sum: 9ee2a4f851141a69af184ac74dfa6c57

Pseudo is Ultrasoft + core correction, Zval = 11.0

Generated using "atomic" code by A. Dal Corso v.5.0.2 svn rev. 9415

Using radial grid of 1279 points, 6 beta functions with:

l(1) = 0

l(2) = 0

l(3) = 1

l(4) = 1

l(5) = 2

l(6) = 2

Q(r) pseudized with 0 coefficients

PseudoPot. # 2 for Cu read from file:

/home/mujahid/Downloads/espresso-4.3.2/pseudo/Cu.pbe-kjpaw.UPF

MD5 check sum: 92cd914fcb04cfd737edc2091ad11b5d

Pseudo is Projector augmented-wave + core cor, Zval = 11.0

Generated using "atomic" code by A. Dal Corso (espresso distribution)

Shape of augmentation charge: BESSEL

Using radial grid of 1199 points, 6 beta functions with:

l(1) = 2

l(2) = 2

l(3) = 0

l(4) = 0

l(5) = 1

l(6) = 1

Q(r) pseudized with 0 coefficients

atomic species	valence	mass	pseudopotential
Au	11.00	1.00000	Au(1.00)
Cu	11.00	1.00000	Cu(1.00)

6 Sym. Ops. (no inversion) found

Cartesian axes

site n.	atom	positions (alat units)
1	Au	tau(1) = (-1.0000000 -1.0000000 -0.8218190)
2	Au	tau(2) = (-1.0000000 -0.8218190 -1.0000000)
3	Au	tau(3) = (-1.0000000 -0.8218190 -0.6436370)
4	Au	tau(4) = (-1.0000000 -0.6436370 -0.8218190)
5	Au	tau(5) = (-0.8218190 -1.0000000 -1.0000000)
6	Au	tau(6) = (-0.8218190 -1.0000000 -0.6436370)
7	Au	tau(7) = (-0.6436370 -1.0000000 -0.8218190)
8	Au	tau(8) = (-0.8218190 -0.6436370 -1.0000000)

```
 9          Au  tau(   9) = (  -0.6436370  -0.8218190  -1.0000000  )
10          Cu  tau(  10) = (  -0.8218190  -0.8218190  -0.8218190  )
11          Au  tau(  11) = (  -0.8218190  -0.6436370  -0.6436370  )
12          Au  tau(  12) = (  -0.6436370  -0.8218190  -0.6436370  )
13          Au  tau(  13) = (  -0.6436370  -0.6436370  -0.8218190  )

number of k points=     4  Methfessel-Paxton smearing, width (Ry)=  0.0500
                cart. coord. in units 2pi/alat
  k(    1) = (   0.0000000   0.0000000   0.0000000), wk =   0.2500000
  k(    2) = (   0.5000000   0.0000000   0.0000000), wk =   0.7500000
  k(    3) = (   0.5000000   0.5000000   0.0000000), wk =   0.7500000
  k(    4) = (   0.5000000   0.5000000   0.5000000), wk =   0.2500000

Dense  grid:   342243 G-vectors     FFT dimensions: (  90,  90,  90)

Estimated max dynamical RAM per process >       1.64 GB

Initial potential from superposition of free atoms
Check: negative starting charge=   -0.076785

starting charge  142.99841, renormalised to  143.00000

negative rho (up, down):  7.679E-02 0.000E+00
Starting wfc are  117 randomized atomic wfcs

total cpu time spent up to now is       29.2 secs

Self-consistent Calculation

iteration #  1     ecut=    40.00 Ry     beta= 0.30
Davidson diagonalization with overlap
ethr =  1.00E-02,  avg # of iterations =  3.0
```

Threshold (ethr) on eigenvalues was too large:
Diagonalizing with lowered threshold

Davidson diagonalization with overlap
ethr = 4.81E-04, avg # of iterations = 3.5

negative rho (up, down): 7.496E-02 0.000E+00

total cpu time spent up to now is 138.5 secs

total energy = -1236.78345318 Ry
Harris-Foulkes estimate = -1237.25748951 Ry
estimated scf accuracy < 0.81247515 Ry

iteration # 2 ecut= 40.00 Ry beta= 0.30
Davidson diagonalization with overlap
ethr = 5.68E-04, avg # of iterations = 4.0

negative rho (up, down): 7.565E-02 0.000E+00

total cpu time spent up to now is 197.0 secs

total energy = -1237.04777162 Ry
Harris-Foulkes estimate = -1237.33307610 Ry
estimated scf accuracy < 0.61934367 Ry

iteration # 3 ecut= 40.00 Ry beta= 0.30
Davidson diagonalization with overlap
ethr = 4.33E-04, avg # of iterations = 3.0

negative rho (up, down): 7.656E-02 0.000E+00

total cpu time spent up to now is 254.4 secs

total energy = -1237.08865172 Ry
Harris-Foulkes estimate = -1237.12490360 Ry
estimated scf accuracy < 0.05468425 Ry

iteration # 4 ecut= 40.00 Ry beta= 0.30
Davidson diagonalization with overlap
ethr = 3.82E-05, avg # of iterations = 4.8

negative rho (up, down): 7.774E-02 0.000E+00

total cpu time spent up to now is 316.9 secs

total energy = -1237.08897336 Ry
Harris-Foulkes estimate = -1237.11833219 Ry
estimated scf accuracy < 0.08786672 Ry

iteration # 5 ecut= 40.00 Ry beta= 0.30
Davidson diagonalization with overlap
ethr = 3.82E-05, avg # of iterations = 4.0

negative rho (up, down): 8.052E-02 0.000E+00

total cpu time spent up to now is 375.9 secs

total energy = -1237.10576777 Ry
Harris-Foulkes estimate = -1237.11369961 Ry
estimated scf accuracy < 0.01222624 Ry

iteration # 6 ecut= 40.00 Ry beta= 0.30
Davidson diagonalization with overlap
ethr = 8.55E-06, avg # of iterations = 4.0

negative rho (up, down): 8.234E-02 0.000E+00

total cpu time spent up to now is   437.0 secs

total energy   =   -1237.10874653 Ry
Harris-Foulkes estimate   =   -1237.11270185 Ry
estimated scf accuracy   <   0.00898304 Ry

iteration # 7   ecut=   40.00 Ry   beta= 0.30
Davidson diagonalization with overlap
ethr = 6.28E-06, avg # of iterations = 4.0

negative rho (up, down): 8.280E-02 0.000E+00

total cpu time spent up to now is   496.0 secs

total energy   =   -1237.11134930 Ry
Harris-Foulkes estimate   =   -1237.11134596 Ry
estimated scf accuracy   <   0.00065028 Ry

iteration # 8   ecut=   40.00 Ry   beta= 0.30
Davidson diagonalization with overlap
ethr = 4.55E-07, avg # of iterations = 2.0

negative rho (up, down): 8.317E-02 0.000E+00

total cpu time spent up to now is   547.9 secs

total energy   =   -1237.11120905 Ry
Harris-Foulkes estimate   =   -1237.11137683 Ry
estimated scf accuracy   <   0.00090932 Ry

iteration # 9   ecut=   40.00 Ry   beta= 0.30

Davidson diagonalization with overlap
ethr = 4.55E-07, avg # of iterations = 2.0

negative rho (up, down): 8.379E-02 0.000E+00

total cpu time spent up to now is 601.1 secs

total energy = -1237.11115021 Ry
Harris-Foulkes estimate = -1237.11124757 Ry
estimated scf accuracy < 0.00024043 Ry

iteration # 10 ecut= 40.00 Ry beta= 0.30
Davidson diagonalization with overlap
ethr = 1.68E-07, avg # of iterations = 3.0

negative rho (up, down): 8.413E-02 0.000E+00

total cpu time spent up to now is 661.2 secs

total energy = -1237.11121815 Ry
Harris-Foulkes estimate = -1237.11122521 Ry
estimated scf accuracy < 0.00002317 Ry

iteration # 11 ecut= 40.00 Ry beta= 0.30
Davidson diagonalization with overlap
ethr = 1.62E-08, avg # of iterations = 4.0

negative rho (up, down): 8.426E-02 0.000E+00

total cpu time spent up to now is 725.0 secs

total energy = -1237.11123225 Ry
Harris-Foulkes estimate = -1237.11123062 Ry

estimated scf accuracy < 0.00000775 Ry

iteration # 12 ecut= 40.00 Ry beta= 0.30
Davidson diagonalization with overlap
ethr = 5.42E-09, avg # of iterations = 4.0

negative rho (up, down): 8.402E-02 0.000E+00

total cpu time spent up to now is 785.4 secs

total energy = -1237.11117406 Ry
Harris-Foulkes estimate = -1237.11123469 Ry
estimated scf accuracy < 0.00000116 Ry

iteration # 13 ecut= 40.00 Ry beta= 0.30
Davidson diagonalization with overlap
ethr = 8.13E-10, avg # of iterations = 4.0

negative rho (up, down): 8.421E-02 0.000E+00

total cpu time spent up to now is 860.8 secs

total energy = -1237.11120670 Ry
Harris-Foulkes estimate = -1237.11120972 Ry
estimated scf accuracy < 0.00000363 Ry

iteration # 14 ecut= 40.00 Ry beta= 0.30
Davidson diagonalization with overlap
ethr = 8.13E-10, avg # of iterations = 3.0

negative rho (up, down): 8.445E-02 0.000E+00

total cpu time spent up to now is 927.7 secs

total energy = -1237.11120102 Ry
Harris-Foulkes estimate = -1237.11120819 Ry
estimated scf accuracy < 0.00000121 Ry

iteration # 15 ecut= 40.00 Ry beta= 0.30
Davidson diagonalization with overlap
ethr = 8.13E-10, avg # of iterations = 3.0

negative rho (up, down): 8.478E-02 0.000E+00

total cpu time spent up to now is 995.8 secs

End of self-consistent calculation

k = 0.0000 0.0000 0.0000 (42931 PWs) bands (ev):

-8.0574 -6.6551 -6.6551 -6.6551 -6.4091 -6.3230 -6.3230 -6.3230
-6.1890 -5.9248 -5.9248 -5.8019 -5.8019 -5.8019 -5.7815 -5.7815
-5.7815 -5.5929 -5.5304 -5.5304 -5.3728 -5.3728 -5.3728 -5.3617
-5.3617 -5.3616 -5.0193 -5.0193 -5.0193 -4.8959 -4.8959 -4.8959
-4.8353 -4.8353 -4.8353 -4.4264 -4.4264 -4.3914 -4.3914 -4.3914
-4.2342 -4.2342 -4.2342 -3.9942 -3.9942 -3.9752 -3.9752 -3.9752
-3.7895 -3.7895 -3.7622 -3.7621 -3.7621 -3.7606 -3.7606 -3.7606
-3.6846 -3.6358 -3.6358 -3.6358 -3.5567 -3.5566 -3.5566 -3.5234
-3.5234 -3.5234 -3.5073 -3.5073 -3.0459 -2.3814 -2.3814 -2.3814
-1.7078 -1.7078 -0.8804 -0.2154 -0.2153 -0.2153 0.2958 0.9416
0.9416 0.9416 1.7014 1.7015 1.7015 2.3151

k = 0.5000 0.0000 0.0000 (42828 PWs) bands (ev):

-8.0571 -6.6560 -6.6548 -6.6548 -6.4090 -6.3232 -6.3231 -6.3230
-6.1890 -5.9248 -5.9246 -5.8021 -5.8021 -5.8018 -5.7816 -5.7813

-5.7813 -5.5917 -5.5305 -5.5304 -5.3731 -5.3727 -5.3727 -5.3618
-5.3615 -5.3614 -5.0195 -5.0195 -5.0193 -4.8962 -4.8962 -4.8959
-4.8386 -4.8352 -4.8352 -4.4262 -4.4261 -4.3916 -4.3916 -4.3914
-4.2354 -4.2341 -4.2341 -3.9941 -3.9920 -3.9753 -3.9752 -3.9752
-3.7898 -3.7896 -3.7634 -3.7634 -3.7621 -3.7608 -3.7586 -3.7586
-3.6841 -3.6360 -3.6359 -3.6358 -3.5688 -3.5554 -3.5554 -3.5236
-3.5236 -3.5231 -3.5070 -3.5070 -3.0459 -2.3955 -2.3955 -2.3800
-1.7014 -1.6608 -0.8157 -0.2473 -0.1840 -0.1840 0.2771 0.7802
1.0577 1.0578 1.2464 1.7114 1.7114 2.3058

k = 0.5000 0.5000 0.0000 (42748 PWs) bands (ev):

-8.0567 -6.6557 -6.6557 -6.6546 -6.4088 -6.3233 -6.3231 -6.3231
-6.1891 -5.9247 -5.9245 -5.8024 -5.8021 -5.8021 -5.7813 -5.7813
-5.7811 -5.5904 -5.5305 -5.5304 -5.3729 -5.3729 -5.3725 -5.3616
-5.3615 -5.3613 -5.0198 -5.0195 -5.0195 -4.8965 -4.8961 -4.8961
-4.8385 -4.8385 -4.8352 -4.4259 -4.4259 -4.3917 -4.3915 -4.3915
-4.2353 -4.2353 -4.2340 -3.9929 -3.9908 -3.9753 -3.9753 -3.9751
-3.7900 -3.7898 -3.7647 -3.7634 -3.7634 -3.7587 -3.7587 -3.7566
-3.6836 -3.6361 -3.6359 -3.6359 -3.5675 -3.5674 -3.5542 -3.5237
-3.5233 -3.5233 -3.5066 -3.5066 -3.0459 -2.4107 -2.3940 -2.3939
-1.6767 -1.6298 -0.7583 -0.2123 -0.2122 -0.1485 0.2555 0.9156
0.9157 1.1710 1.2769 1.2770 1.7210 1.9712

k = 0.5000 0.5000 0.5000 (42584 PWs) bands (ev):

-8.0564 -6.6554 -6.6554 -6.6554 -6.4087 -6.3232 -6.3232 -6.3232
-6.1891 -5.9244 -5.9244 -5.8023 -5.8023 -5.8023 -5.7811 -5.7811
-5.7811 -5.5892 -5.5305 -5.5305 -5.3727 -5.3727 -5.3727 -5.3614
-5.3614 -5.3613 -5.0198 -5.0198 -5.0198 -4.8965 -4.8965 -4.8964
-4.8385 -4.8385 -4.8385 -4.4258 -4.4258 -4.3916 -4.3916 -4.3916
-4.2352 -4.2352 -4.2352 -3.9907 -3.9907 -3.9752 -3.9752 -3.9752
-3.7901 -3.7901 -3.7647 -3.7647 -3.7647 -3.7567 -3.7567 -3.7566

-3.6832 -3.6360 -3.6360 -3.6360 -3.5662 -3.5661 -3.5661 -3.5234
-3.5234 -3.5234 -3.5063 -3.5063 -3.0459 -2.4091 -2.4091 -2.4091
-1.6249 -1.6249 -0.7065 -0.1714 -0.1714 -0.1714 0.2290 1.0354
1.0354 1.0355 1.3156 1.3158 1.3158 2.0926

the Fermi energy is -2.1629 ev

! total energy = -1237.11120660 Ry
Harris-Foulkes estimate = -1237.11120684 Ry
estimated scf accuracy < 0.00000009 Ry

The total energy is the sum of the following terms:
one-electron contribution = -2149.78846576 Ry
hartree contribution = 1143.52563424 Ry
xc contribution = -403.14313901 Ry
ewald contribution = 268.57755254 Ry
one-center paw contrib. = -96.28620224 Ry
smearing contrib. (-TS) = 0.00341362 Ry
convergence has been achieved in 15 iterations
Writing output data file pwscf.save
init_run : 27.68s CPU 28.63s WALL (1 calls)
electrons : 938.50s CPU 966.63s WALL (1 calls)
Called by init_run:
wfcinit : 23.45s CPU 23.70s WALL (1 calls)
potinit : 0.73s CPU 0.76s WALL (1 calls)

Called by electrons:
c_bands : 759.95s CPU 771.98s WALL (16 calls)
sum_band : 145.09s CPU 153.36s WALL (16 calls)
v_of_rho : 7.62s CPU 7.64s WALL (16 calls)
newd : 23.64s CPU 32.02s WALL (16 calls)
PAW_pot : 2.40s CPU 2.40s WALL (16 calls)
mix_rho : 1.70s CPU 1.74s WALL (16 calls)

Called by c_bands:
init_us_2 : 6.65s CPU 6.71s WALL (132 calls)
cegterg : 700.45s CPU 712.43s WALL (64 calls)

Called by sum_band:
sum_band:bec : 0.01s CPU 0.01s WALL (64 calls)
addusdens : 31.71s CPU 39.86s WALL (16 calls)
Called by *egterg:
h_psi : 544.63s CPU 545.11s WALL (289 calls)
s_psi : 50.44s CPU 50.45s WALL (289 calls)
g_psi : 3.14s CPU 3.15s WALL (221 calls)
cdiaghg : 3.88s CPU 3.88s WALL (281 calls)

Called by h_psi:
h_psi:pot : 542.20s CPU 542.62s WALL (289 calls)
h_psi:calbec : 48.15s CPU 48.16s WALL (289 calls)
vloc_psi : 443.67s CPU 444.06s WALL (289 calls)
add_vuspsi : 50.38s CPU 50.39s WALL (289 calls)

General routines
calbec : 66.35s CPU 66.36s WALL (353 calls)
fft : 4.99s CPU 5.00s WALL (210 calls)
fftw : 472.82s CPU 473.26s WALL (33004 calls)

PWSCF : 16m 6.79s CPU 16m36.05s WALL

This run was terminated on: 2:51:43 9Apr2018

=--=
JOB DONE.
=--=